



# Marine Heatwaves across the central South Pacific: characteristics, mechanisms, and modulation by the El Niño Southern Oscillation

Bastien Pagli<sup>1</sup>, Takeshi Izumo<sup>1</sup>, Alexandre Barboni<sup>2</sup>, Carla Chevillard<sup>3</sup>, Cyril Dutheil<sup>4</sup>, Raphaël Legrand<sup>5</sup>, Christophe Menkes<sup>6</sup>, Claire Rocuet<sup>1</sup> and Sophie Cravatte<sup>7</sup>

<sup>1</sup>UMR 241 SECOPOL, (IRD, ILM, Ifremer, UPF), Tahiti, French Polynesia

<sup>2</sup>Laboratoire d'Etudes en Géophysique et Océanographie Spatiales (LEGOS), Toulouse, France

<sup>3</sup>IFREMER, Tahiti, French Polynesia

<sup>4</sup>MARBEC, University of Montpellier, CNRS, Ifremer, IRD, Sète, France

<sup>5</sup>DIRPF, Météo France, Tahiti, French Polynesia

<sup>6</sup>ENTROPIE (IRD, Ifremer, Université de la Réunion, Université de la Nouvelle-Calédonie), Nouméa, New Caledonia

<sup>7</sup>Université de Toulouse, LEGOS (IRD, CNES, CNRS, UT3), Toulouse, France.

Correspondence to: Bastien Pagli (bastien.pagli@ird.fr)

**Abstract.** Marine heatwaves (MHWs) are intensifying with climate change, endangering ecosystems such as coral reefs. Yet their regional characteristics and drivers remain poorly understood in many parts of the Pacific. Here we provide a comprehensive assessment of MHWs in the central South Pacific and across the five archipelagos of French Polynesia (representing ~77 atolls, more than half of world's atolls, and more than 5 million km<sup>2</sup> of maritime area, a region as vast as Europe), using sea surface temperature observations and an ocean reanalysis to investigate underlying mechanisms. MHW exposure varies widely across the region: its northern and southern parts (the Marquesas and Austral archipelagos respectively) experience the highest number of MHW days and the strongest cumulative intensities, especially during the warm season (Nov-Apr). In contrast, its central part (the Society, Tuamotu, and Gambier Islands) exhibits more moderate MHW characteristics. Heat budget analyses highlight the seasonally and regionally diverse mechanisms shaping MHWs. In central FP during the warm season, most of MHWs are driven by air-sea heat fluxes, while in the northern part, those driven by oceanic horizontal advection dominate. During the cold season, more MHWs driven by horizontal advection are observed in the whole region since the thicker seasonal mixed layer reduce the proportion of MHWs driven by air-sea fluxes. El Niño–Southern Oscillation (ENSO) strongly modulates MHWs occurrence: El Niño favors MHWs occurrence in northeastern FP, while La Niña increases MHW occurrence in the southwest with different spatial extent across ENSO flavors (Central and Eastern Pacific ENSO events). This modulation arises from reduced wind-evaporation cooling with reduced wind speed, shoaled mixed layers, and enhanced horizontal heat advection. These results greatly improve our understanding of MHW characteristics, dynamics and variability in this ecologically-fragile region.



## 32 1- Introduction

33 Marine heatwaves (MHWs), known as prolonged periods of extreme ocean temperature, have significant impacts on marine  
 34 ecosystems and, consequently, on island communities that rely on ecosystem services, fisheries, and tourism. Their  
 35 frequency and duration have increased over recent decades due to global ocean warming and are projected to continue rising  
 36 in the future (Oliver et al., 2018). Developing skillful forecasts of MHWs is therefore essential for mitigating their impacts.  
 37 Such forecasts depend on a robust understanding of MHW characteristics, their mechanisms, their physical drivers, and their  
 38 variability. None of these aspects has yet been studied in detail over the French Polynesia (FP) region where MHWs can lead  
 39 to severe socioeconomic consequences (Hédouin et al., 2020).

40 Some initial results regarding the mean characteristics and the dominant climate modes driving the MHWs can be extracted  
 41 from past studies conducted at broader spatial scales, such as the South Pacific or even globally. In the South-Central Pacific,  
 42 El Niño Southern Oscillation (ENSO) with its different phases El Niño (EN) and La Niña (LN) are known to be important  
 43 drivers of increased MHW occurrence (Holbrook et al., 2019, 2022) and MHW intensity (Sen Gupta et al., 2020).  
 44 Additionally, the different flavors of ENSO (Capotondi et al., 2020) exhibit distinct connections with MHWs across the  
 45 Pacific Ocean in terms of both intensity and likelihood. Using Linear Inverse Model (LIM) data, (Gregory et al., (2024)  
 46 showed that these relationships vary between the Eastern Pacific (EP) and Central Pacific (CP) flavors of EN and LN. In the  
 47 tropical Pacific, both MHW intensity occurrence tend to be consistent with SST anomalies during ENSO events, with  
 48 maxima occurring in the central Pacific during CP EN events and in the eastern Pacific during EP EN events.

49 Regarding the mechanisms of MHWs, global studies generally rely on numerical models to estimate the main physical  
 50 processes driving MHWs globally (Marin et al., 2022; Vogt et al., 2022; Bian et al., 2023, 2024). These studies aim at  
 51 identifying the dominant mechanisms during MHWs among oceanic heat advection, air/sea heat flux, horizontal and vertical  
 52 mixing and entrainment at the mixed layer base depending on the methods used to calculate mixed layer heat budgets during  
 53 MHWs. The dominant mechanisms during the MHWs onset and decay are region dependent (Elzahaby et al., 2022; Bian et  
 54 al., 2023) and also spatial model resolution dependent due to the resolution or not of oceanic eddies by the model (Bian et  
 55 al., 2024). This highlights the need for regional studies to better understand MHWs (e.g. Schlegel et al., 2021; Elzahaby et  
 56 al., 2021; Dutheil et al., 2024; Lal et al., 2025).

57 In austral summer (from November to April), which is the time of the year where ENSO events generally reach their peak of  
 58 intensity, ENSO strongly modifies SST, ocean currents, precipitation, and wind over FP compared to climatology. Opposite  
 59 impacts across different parts of the country are observed depending on the ENSO flavor, due to FP geographical position  
 60 often close to ENSO SST anomalies edges and its effect on the South Pacific Convergence Zone (SPCZ) position (Vincent et  
 61 al., 2011; Pagli et al., 2025a). EN (LN) events typically warm (cool) the northeastern half of FP while cooling (warming) the  
 62 southwestern half, though the boundaries and intensity of these anomalies vary by ENSO flavor. During extreme EP EN  
 63 events, a strong northeastward migration of the SPCZ (Vincent et al., 2011) induces enhanced precipitation and cloud cover  
 64 in the northern half of FP, with intensified westerly wind anomalies. This impacts Ekman pumping and thermocline depth,



65 weakens the westward South Equatorial Current (SEC) and strengthens the South Equatorial Countercurrent (SECC)  
 66 (Martinez et al., 2009). In contrast, CP EN events cause a more moderate northeastward SPCZ shift relative to its mean  
 67 position and weaker surface winds over central FP. Moderate-to-strong LN events shift the SPCZ southwest, reducing cloud  
 68 cover and enhancing trade winds, strengthening the SEC and weakening the SECC. These changes are amplified during very  
 69 strong LN episodes (Pagli et al., 2025a). Overall, ENSO modulates surface ocean and atmospheric conditions, altering the  
 70 large-scale background state in which MHWs may develop.

71 The aim of this study is to analyze in detail past oceanic MHWs over FP in order to address the following questions: What  
 72 are the characteristics of past MHWs over FP and across the archipelagos? To what extent does ENSO drive, or modulate  
 73 these extreme events and their dynamics? What are the local mechanisms responsible for the onset/ decay of these events  
 74 across the area?

75 Section 2 describes the data and methods used to address these questions. Section 3 presents the characteristics of past  
 76 MHWs over FP, while section 4 explores their modulation by ENSO. Section 5 investigates the underlying mechanisms  
 77 driving these MHWs, and sections 6 and 7 provide the conclusions and discussion.

78

## 79 **2- Data and Methods**

### 80 **2.1-Data and model simulations**

81 Daily SST data were obtained from the OISSTv2 dataset, a blend of in situ and satellite observations (Huang et al., 2021),  
 82 covering the period from 1981 (01 Sept) to 2024 (31 Dec) on a  $0.25^\circ$  resolution grid. The mechanisms driving the MHWs  
 83 detected over FP were investigated using the global eddy-resolving  $1/12^\circ$  ocean reanalysis GLORYS12v1 (Lellouche et al.,  
 84 2021), hereafter named GLORYS. In GLORYS the ocean and sea ice general circulation model is NEMO (Madec et al.,  
 85 2024). Daily oceanic variables—including potential temperature, mixed layer depth, zonal and meridional currents—were  
 86 analyzed. In addition, surface heat and momentum fluxes used to force the oceanic model (including the large-scale  
 87 corrections applied by Lellouche et al., 2021), were analyzed. GLORYS reanalysis is forced by ERA-Interim until 2019  
 88 (Dee et al., 2011) and ERA5 afterwards (Hersbach et al., 2020). Due to the known large biases in radiative fluxes at the  
 89 surface in ERA-Interim, large-scale corrections were made using the NASA/GEWEX Surface Radiation Budget 3.0/3.1  
 90 product (Stackhouse et al., 2021) for shortwave and longwave fluxes (Lellouche et al., 2021). Along track altimeter sea-level  
 91 anomaly, satellite sea surface temperature (AVHRR SST from NOAA) and sea-ice concentration (Ifremer/CERSAT) as well  
 92 as in situ temperature and salinity vertical profiles (CORA database from CMEMS) are assimilated in GLORYS. Tides are  
 93 not represented explicitly in GLORYS (Lellouche et al., 2018). Because of data assimilation, the heat and momentum  
 94 budgets are not closed in GLORYS but previous studies showed its realism for analyzing MHW heat budget in the South  
 95 Pacific (Dutheil et al., 2024).



MHW detection was performed using both OISSTv2 (from 1981 to 2024) and GLORYS (from 1993 to 2024). However, the mixed layer heat budget in GLORYS (see Methods) was limited to the period from 1993 to 2020 due to the forcing fields (momentum and heat fluxes) data availability. For consistency with the OISST results, GLORYS fields were regridded onto the spatial grid of the OISST dataset at 0.25° using a first order conservative remapping method.

## 2.2-Methods

### MHW detection

MHWs were detected in the OISSTv2 dataset, and independently in the GLORYS reanalysis over the FP domain (165°W–130°W, 30°S–0°S) for the period 1981–2024 (respectively 1993–2024), following the method described by Hobday et al., (2016). For each product, we used the 1993–2020 period as the climatological baseline. At each grid point, a MHW was identified when daily SST exceeded the 90th seasonally varying percentile ( $SST^{90th}$ ) (cf. Fig. S1 for warm and cold seasons average of the threshold over FP) for at least five consecutive days.  $SST^{90th}$  were computed with a moving 11-day window to ensure enough daily SST samples for a robust 90th-percentile estimate. A 31-day smoothing filter was then applied to remove high-frequency noise. The same filter has been used for the SST climatology. Events separated by fewer than two days were considered as a single continuous event. Standard metrics were then calculated for each MHW, following the methodology of Hobday et al. (2016). These include the number of events, maximum, mean, and cumulative intensity, duration, onset and decline rates (defined as the mean SST change from start to peak and from peak to end, respectively), and the gaps between events. MHW intensity can be expressed either in absolute terms (i.e., the actual SST) or relative to the mean climatological baseline. MHWs were detected independently at each grid point; no spatial connectivity was assumed between neighboring points. Nevertheless, a daily analysis of MHW occurrence across the domain was conducted to identify connected MHW areas (Lal et al., 2025). At each daily timestep, connected MHW pixels were labeled, and the area of each labeled object was calculated. For each pointwise-detected MHW, the mean and maximum spatial extent of the labeled object it belonged to were calculated over the event's duration. In the various sections, a distinction is made between MHWs occurring during the austral winter and those occurring during the austral summer, according to the date of their peak intensity.

The severity index ( $S$ ) introduced by Sen Gupta et al., (2020) was also computed on a daily basis in OISSTv2:

$$Severity\ Index\ (S) = \frac{SST - SST_{clim}}{SST^{90th} - SST_{clim}} \quad (1)$$

where  $SST_{clim}$  is the SST climatology.  $S > 1$  indicates that SST exceeds the 90th percentile (i.e.,  $SST > SST^{90th}$ ), while  $0 < S < 1$  reflects SST values warmer than the seasonal average but not exceeding the threshold. Conversely,  $S < 0$  denotes cooler-than-average SST climatology. The severity of MHWs is generally described by values of  $S$  (Hobday et al., 2018). A MHW is categorized as moderate ( $1 < S \leq 2$ ), strong ( $2 < S \leq 3$ ), severe ( $3 < S \leq 4$ ) or extreme ( $S \geq 4$ ).





127

128 In order to quantify the variability of the cumulative heat stress felt by the marine ecosystems, the daily Degree-Heating  
 129 Weeks (DHW) were computed for each austral summer from 1981 to 2024 following Skirving et al., (2020). First, daily  
 130 temperature anomalies (HotSpot) were computed relative to the local Maximum of Monthly Mean (MMM), defined as the  
 131 climatological maximum of monthly mean temperatures computed over the baseline period. DHW on each day were then  
 132 estimated by summing the daily HotSpot anomalies exceeding 1 °C over the preceding 12 weeks (84 days). This  
 133 accumulated value was divided by seven to express DHW in °C-weeks.

134 Results were presented as averaged for the entire FP domain, and for each of the five main archipelagos: the Marquesas,  
 135 Tuamotu, Society, Gambier, and Austral Islands. The regions associated with each archipelago, over which MHW metrics  
 136 were aggregated, were defined based on [https://www.data.gouv.fr/fr/datasets/geographie-administrative-de-la-polynesie-](https://www.data.gouv.fr/fr/datasets/geographie-administrative-de-la-polynesie-francaise/)  
 137 [francaise/](https://www.data.gouv.fr/fr/datasets/geographie-administrative-de-la-polynesie-francaise/).

138 Whether or not removing a long term temperature trend (shown in Fig. S2 for FP region) before applying the detection  
 139 method is a methodological choice, which can influence the results and their significance (Amaya et al., 2023; Capotondi et  
 140 al., 2024). Both approaches are complementary, and the most appropriate depends on the specific research question to  
 141 address. Retaining the trend, and estimating the “total heat exposure”, is more suitable when assessing the impacts of MHWs  
 142 on human societies and marine ecosystems, as it reflects the thermal conditions actually experienced. Conversely, when  
 143 investigating interannual variability, links with climate modes, or the underlying mechanisms driving MHWs, removing the  
 144 trend can be useful to better isolate these signals. For this reason, the part that describes the MHWs metrics over FP was  
 145 made without removing the trend (section 3) and the part analyzing the link with ENSO and the mechanisms of MHW was  
 146 made with detrended SST data (section 4-5). For section 3, complementary results based on detrended SST data—where the  
 147 MHW detection method and threshold computation were reapplied—are provided in the Supplementary Information (SI).  
 148 Briefly, detrending does not alter the main results — such as differences between archipelagos, ENSO modulation, dominant  
 149 mechanisms — but does slightly affect some quantitative MHW characteristics, including their duration, intensity, and  
 150 onset/decline rates.

151

## 152 **MHW/ENSO relationships**

153 The link between MHWs and ENSO was examined at two levels of complexity. First, MHW occurrence across FP in all  
 154 seasons was analyzed separately for EN, LN, and N phases, based on the Oceanic Niño Index (ONI; NOAA), using the  
 155 criterion that EN (respectively LN) conditions corresponded to  $ONI > 0.5$  ( $< -0.5$ ) for at least five consecutive months (see  
 156 Fig. S3 for the different periods considered as EN and LN). Second, ENSO diversity was considered using the FP-specific  
 157 classification developed by Pagli et al. (2025a). This classification identified six ENSO clusters based on interannual relative  
 158 SST anomalies, precipitation (PR), and 850 hPa zonal wind (U850) averaged over the austral summer: three EN types  
 159 (Extreme EP, Strong Mixed, and CP), one Neutral (N)/weak EP LN group (EPLN+N), and two LN types (CP and Strong  
 160 Mixed). The classified years are presented in Table S1 (including the 2023-2024 strong Mixed EN event, cf. Pagli et al.



2025b). For this classification, the analysis of MHW–ENSO relationships was restricted to the austral summer. MHW characteristics were composited for each of the six ENSO groups. For each ENSO cluster, both the S index and percentage of days with  $S \geq 1$  were computed over the FP domain. The maximum of DHW reached over the warm season was also computed each year and composited by ENSO clusters.

### Mixed layer heat budget and MHW category

The mechanisms of MHWs were investigated through a mixed layer heat budget analysis performed in GLORYS based on the following equation (Moisan and Niiler, 1998; Oliver et al., 2021; Dutheil et al., 2024):

$$\underbrace{\frac{\partial \langle T \rangle'}{\partial t}}_{\text{tendency}} = \underbrace{-\langle \mathbf{U} \rangle \cdot \nabla \langle T \rangle'}_{\text{Horizontal advection HADV}} + \underbrace{\left( \frac{Q_{\text{net}}}{\rho c_p h} \right)'}_{\text{Air-sea heat flux } Q} + \underbrace{\text{Residual}}_{\text{RES}} \quad (2)$$

with

$$\begin{aligned} \text{Residual} = & \underbrace{\langle \nabla \cdot (\kappa_h \nabla T) \rangle}_{\text{Horizontal mixing}} - \underbrace{\frac{1}{h} \kappa_z \frac{\partial T}{\partial z} \Big|_{-h}}_{\text{Vertical mixing}} - \underbrace{\left( \frac{\langle T \rangle - T_{-h}}{h} \right) \left( \frac{\partial h}{\partial t} + \mathbf{U}_{-h} \cdot \nabla h + w_{-h} \right)}_{\text{Entrainment}} \\ & + \underbrace{DA}_{\text{Data assimilation increments}} \end{aligned} \quad (3)$$

where  $\rho = 1027 \text{ kg/m}^3$  is the mean density of sea water,  $c_p = 4187 \text{ J} \cdot \text{K}^{-1} \cdot \text{kg}^{-1}$  is the specific heat capacity of seawater,  $\kappa_h$  and  $\kappa_z$  are the horizontal and vertical diffusivity coefficients in  $\text{m}^2/\text{s}$ ,  $h$  is the mixed layer depth in m (defined as the depth where the density increase compared to density at 10 m depth corresponds to a temperature decrease of  $0.2^\circ\text{C}$ ),  $T$  is the temperature in the mixed layer in K,  $\mathbf{U}$  is the horizontal current and  $w$  is the vertical velocity component both in  $\text{m/s}$ ,  $Q_{\text{net}}$  is the net air-sea heat flux in  $\text{W/m}^2$ . Brackets  $\langle \cdot \rangle$  indicate the vertical averaging from the surface to the mixed layer depth. The subscript  $h$  indicates the evaluation of the expression at the mixed layer depth. Each term of Eq (2-3) correspond to anomalies with respect to the daily climatology (as indicated by the prime) computed over 1993–2020. We chose here to consider a time-space varying MLD (and not a fixed seasonal or spatial average) as it has been shown that the identification of the dominant mechanisms at play during MHWs can change depending on the different MLD values when fixing a constant MLD (Elzahaby et al., 2022).

The net surface air/sea flux  $Q_{\text{net}}$  (counted as positive towards the ocean and expressed in  $\text{W} \cdot \text{m}^{-2}$ ) can be decomposed as:

$$Q_{\text{net}} = SW + LHF + SHF + LW - SW(-h) \quad (4)$$

where  $SW$  is the net shortwave flux at the surface,  $SW(-h)$  the shortwave flux leaving at the base of the mixed layer (parametrized following Paulson and Simpson, 1977 for type I water),  $LHF$  the latent heat flux,  $SHF$  the sensible heat flux,



and  $LW$  the longwave radiation flux. Concerning the residual, it encompasses several processes including : the effects of data assimilation, the entrainment at the base of the mixed layer (accounting for its space–time variability, vertical advection and lateral induction), and the horizontal/vertical turbulent mixing (see Eq. 3). However, this residual is generally dominated by vertical mixing (e.g. Dutheil et al., 2024). To quantify the contribution of each term during MHW events in terms of temperature evolution, the heat budget equation was integrated in time during the MHW from the event start ( $t_s$ ):

$$\langle T \rangle'(t) - \langle T \rangle'(t_s) = \int_{t_s}^t \langle \mathbf{U} \rangle \cdot \nabla \langle T \rangle' dk + \int_{t_s}^t \frac{Q_{net}'}{\rho c_p h} dk + \int_{t_s}^t Residual dk \quad (5)$$

Following Elzahaby et al. (2022), at the peak time of each MHW, the contributions (integrated in time) of each term were assessed and compared to determine which term was dominant. Events were then categorized according to the dominant mechanism: **Q-MHW** when air-sea fluxes dominated, **HADV-MHW** when horizontal advection was dominant, **RES-MHW** when the residual term was dominant compared to  $Q$  and  $HADV$  contribution separately as well as their sum, and **Mixed-MHW** when the relative difference between the  $Q$  and  $HADV$  contributions was less than 10% of the total change of temperature from start to peak, and when their combined contribution was less than that of the residual term.

To better understand the mechanisms controlling MHW onset and decay, the different terms of Eqs. (2) and (4), as well as wind (speed and direction), MLD, sea-level (SSH) and surface oceanic currents anomalies were averaged over all MHWs of each type occurring during the warm and cold seasons, separately. These averages were computed for both the development phase (from the MHW start time to its peak) and the decay phase (from the peak to the end time). For the decaying phase all MHWs (including HADV,  $Q$  and RES-MHWs) were used to build the composites. The full terms of Eq. (2) for these composites can be found in Appendix A (Fig. A1, A2).

### 3- MHW characteristics across the central South Pacific and FP archipelagos

Figure 1 presents the median characteristics of past MHWs—including their number, intensity, and duration—detected in the central South Pacific from 1981 to 2024 in OISST, shown separately for austral summer and austral winter. For each archipelago, Fig. 2a–d displays the distribution of these characteristics, along with absolute and cumulative intensity, to assess the level of MHW exposure across FP.

The total number of MHW days over the warm seasons of the period, expressed in mean number of MHW days per year is heterogeneous across the region (Fig. 1a). It ranges from 7 to 13 days per year for central regions (Society-Tuamotu-Gambier) and 13 to 18 days per year in the southwestern (Austral) and northeastern regions (near Marquesas) (Fig.1a). During the cold season (Fig. 1d,e,f), most regions experience fewer MHW days compared to the warm season, with the exception of the Austral and Gambier region, where the number of MHW days is comparable between the two seasons.

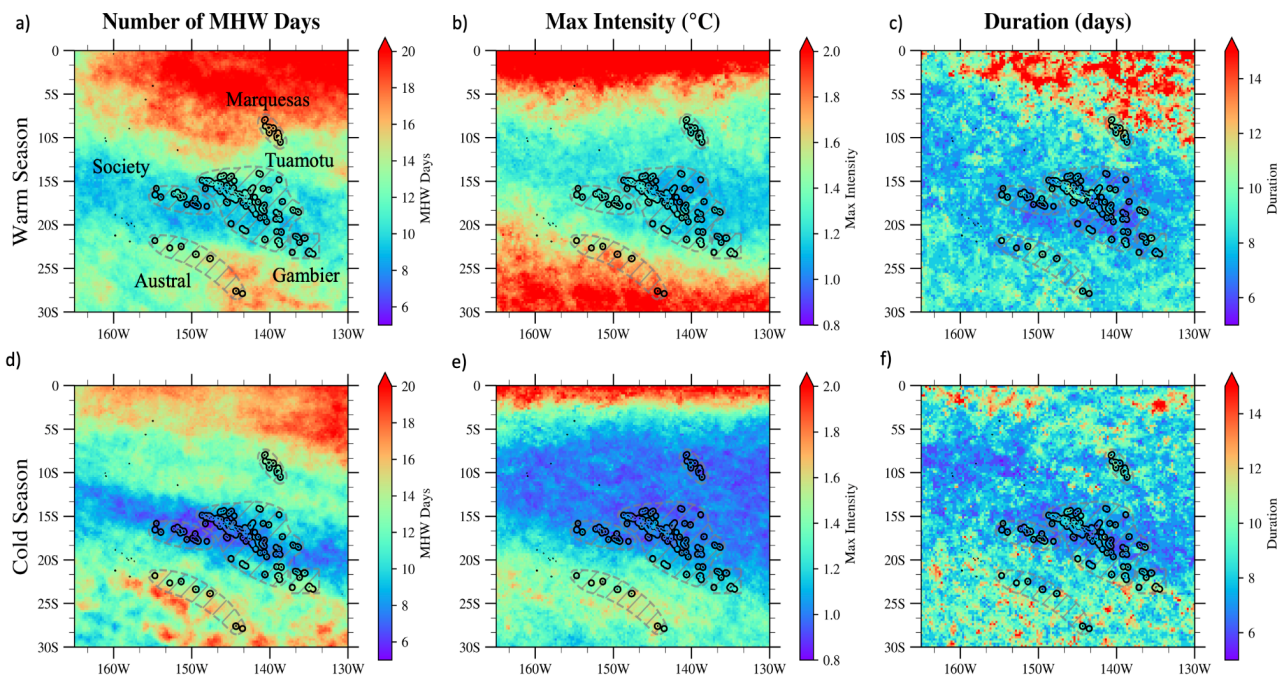


215 The most intense MHWs are observed north of 7°S and south of 25°S (Fig. 1b) leading to median values of +1.7 °C and  
 216 +1.5 °C in the Austral Islands during the warm and cold seasons, respectively (Fig. 2a). In the other archipelagos, median  
 217 intensity values range from +1.0 to +1.3 °C. Across all archipelagos, MHWs are more intense during the warm season than  
 218 during the cold season, both in terms of median and extreme values (Fig. 2a,b). Due to the large meridional extent of FP,  
 219 climatological temperatures vary significantly from south to north (see Fig. S1). Absolute temperatures reached are therefore  
 220 quite different between the Austral and Marquesas. In absolute terms, the most intense heat exposure are found over the  
 221 Society, Tuamotu, and Marquesas archipelagos, with median values ranging from 27.6 to 28.4 °C in the cold season and  
 222 from 29.2 to 29.8 °C in the warm season (Fig. 2b). The most intense heat exposure exceeds 30 °C across most archipelagos  
 223 during both seasons, except in the Gambier Islands (28.8 °C and 29.8 °C for the warm and cold seasons, respectively) and in  
 224 the Austral Islands during the cold season (28.8 °C) (Fig. 2b).

225 The median duration is around 7-10 days for both seasons, with longer duration for the Marquesas region over the warm  
 226 season (Fig. 1c). Most MHW events are short-lived events, across all five archipelagos (Fig. 2d). Longer events are  
 227 particularly frequent in the Marquesas during the austral summer, where 25% of MHWs last longer than 19–20 days, 5% last  
 228 more than 50 days, and the longest MHWs exceed 250 days in both seasons. In the Austral Islands, the upper tail of the  
 229 duration distribution is also shifted upward compared to other archipelagos, with 5% of MHWs lasting more than 45 days in  
 230 both seasons. For the others, 75% of the distribution lies between 10 and 17 days.

231 Cumulative intensity varies across FP in line with intensity and duration distributions (Fig. 2c). The Austral Islands (both  
 232 seasons) and the Marquesas (warm season) experience the highest cumulative intensities, with median values of 10 to  
 233 12 °C·days. In these regions, 25% of MHWs have cumulative impacts exceeding 20 °C·days, and 5% exceed 60 °C·days. In  
 234 the Society, Gambier, and Tuamotu Islands, median cumulative intensities are 7.8, 7.4, and 8.2 °C·days, respectively. In  
 235 these archipelagos, 25% of MHWs exceed 10 °C·days, and 5% exceed 30 °C·days—except in the Society Islands during the  
 236 warm season, where 5% of MHWs exceed 25 °C·days.

237 There is an overall positive trend of the number of MHW days over FP over the period for all archipelagos, as well  
 238 as the area covered by MHWs over the FP region (Fig. 2e). Also, MHWs occurrence vary a lot from year to year, and not the  
 239 same way in each archipelago (Fig. 2e). In the Marquesas, several years may pass with few or no MHW events, followed by  
 240 years with a very high number of MHW days.  
 241 In the Austral Islands, MHWs happen more regularly each year, with some bigger peaks.  
 242 These differences led us to look at the link with ENSO (see Section 4).



243

244

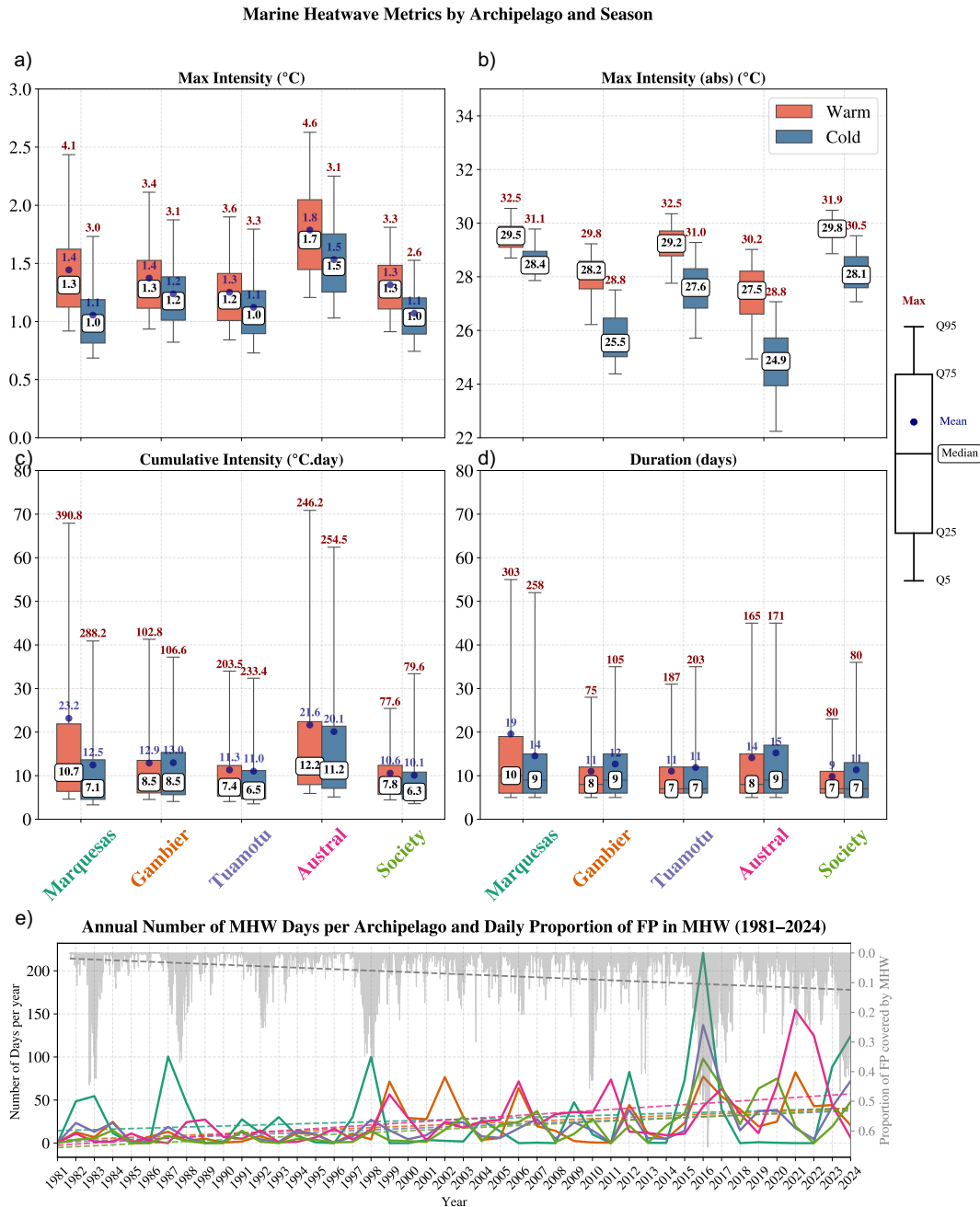
245

246

247

248

**Figure 1.** Median characteristics of MHWs detected over the FP region for the period 1981–2024 in the OISST dataset. The total number of days in MHW expressed in mean number of days per year, maximum intensity (°C), and event duration (days) are displayed for the warm season (NDJFMA) in panels a, b, and c, respectively, and for the cold season (MJJASO) in panels d, e, and f, respectively. The names and locations of the archipelagos are shown in panel (a). The gray dashed areas surrounding each archipelago represent the regions used to group MHW metrics by archipelago in Fig. 2.



249

250 **Figure 2.** Panels (a–d) show MHW metrics’ distributions for each archipelago area (see map on the right ) for warm (NDJFMA, in red)  
251 and cold seasons (MJJASO, in blue). The box plots were generated from all MHW events detected at each grid point within the delimited  
252 regions around each archipelago shown on the Fig. 1a. Panels a–d show, respectively, the maximum intensity reached in each event, its  
253 absolute value, the cumulative intensity, and the duration. The whisker plot limits are indicated on the right side using a labeled box plot  
254 example. Panel (e) displays the annual evolution of the number of MHW days (thick lines) over each archipelago along with their linear  
255 trends (dashed lines). Line colors match the archipelago colors used on the x-axes of panels c and d. The daily proportion of FP covered by  
256 MHWs is shown in light gray, with its corresponding linear trend indicated by a gray dashed line. The slope of the gray dashed line is  
257 0.025 per decade.





258  
 259 Additional metrics, such as onset and decline rate and maximum area, are provided in SI (Fig. S4). MHWs develop and  
 260 decay at a comparable pace across both seasons (MHWs develop slightly faster during the warm season than during the cold  
 261 season, not shown) and all archipelagos, with median growth rates ranging from 0.09 to 0.13 °C/day and decaying rates  
 262 ranging from 0.09 to 0.12 °C/day (Fig. S4a,b). MHWs occurring in the Marquesas tend to have larger spatial extents (median  
 263 of 1.7 million km<sup>2</sup> which is about 20% of the FP maritime Exclusive Economic Zone) compared to those in the Tuamotu,  
 264 Society, Austral, and Gambier Islands, where median values range from 400,000 to 600,000 km<sup>2</sup>. Moreover, large MHWs  
 265 (more than 1M km<sup>2</sup>) are more frequently detected over the Tuamotu and Society Islands than in the Austral and Gambier  
 266 Islands.  
 267 Equivalent analyses of that of Fig. 1 and 2 using the detrended MHW dataset are also available in Fig. S5, S6. In brief,  
 268 detrending the data does not alter the differences observed between archipelagos but slightly reduces MHW intensities across  
 269 all regions, except in the Marquesas where the SST trend is weak and negative (Fig. S2). Detrending also reduces MHW  
 270 duration across all archipelagos. Consequently, cumulative intensity is slightly reduced everywhere except in the Marquesas,  
 271 where it is a bit increased. Additionally, detrending leads to a slight increase in the onset rate of MHWs.  
 272 The same analysis for MHWs detected in GLORYS over 1993-2024 is shown in SI (Fig. S7). For that region, median values  
 273 and inter-archipelagos differences are consistent between OISST and GLORYS. However some differences can be seen,  
 274 detected MHWs are generally longer and weaker in GLORYS than in OISST. Despite these differences, the coherence  
 275 between the products gives us confidence in the ability of GLORYS to simulate the past MHWs realistically.

#### 277 **4- ENSO as a driver of MHWs**

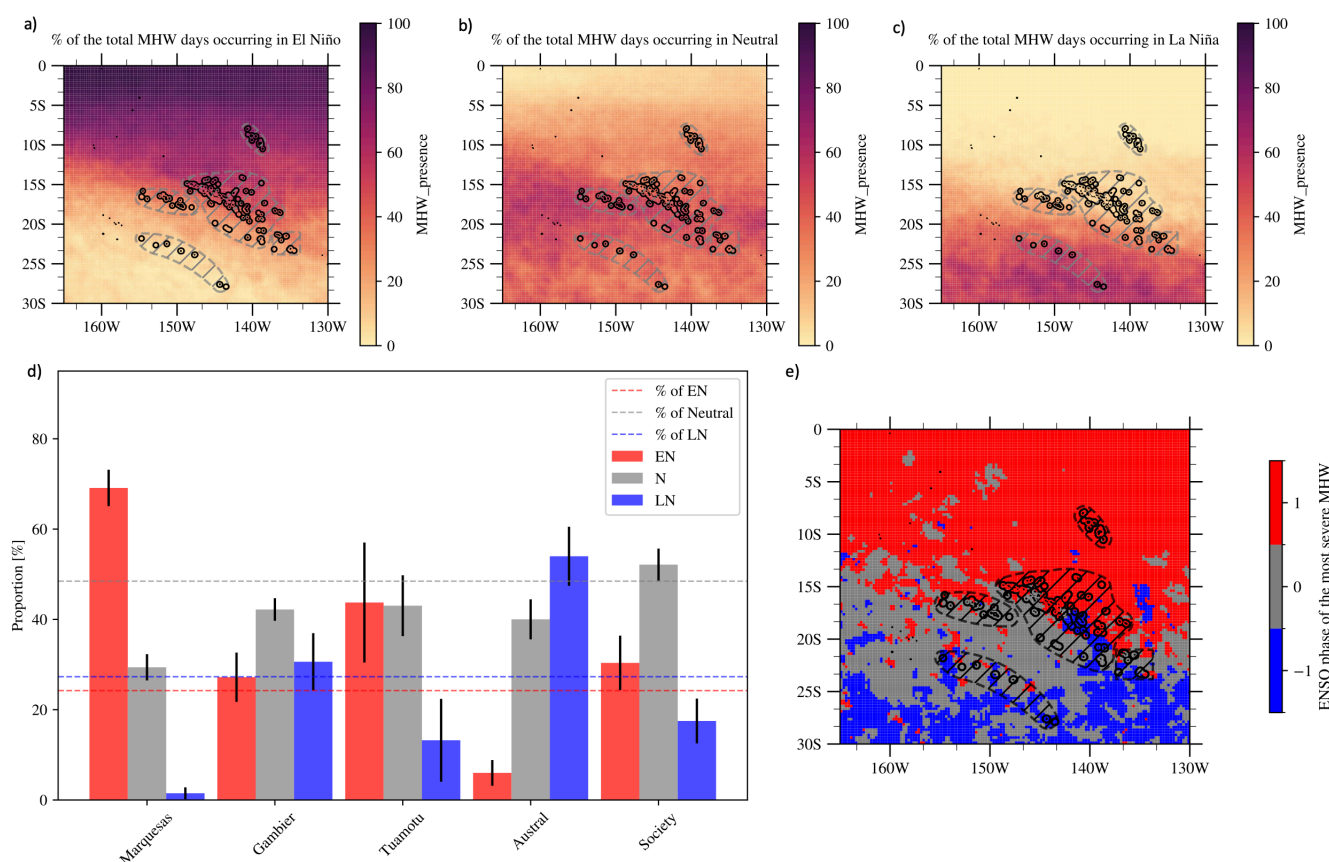
278 We now analyse the link between ENSO and MHWs properties, and examine the modulation of MHWs by ENSO. In section  
 279 4.1, we first simply separated days into EN, LN or N conditions (all seasons taken into account, cf. Methods for  
 280 identification of EN and LN periods). The next section (section 4.2) will discuss ENSO spatial diversity/flavors using Pagli  
 281 et al. (2025a,b) classification. MHWs analyzed here are those detected in the detrended SST of OISST (cf. section 2.2).

##### 282 **4.1- Modulation of MHW occurrence and intensity**

283 Figure 3a–c shows the proportion of MHW days occurring during EN, N, and LN conditions at each grid point. Using the  
 284 proportion of MHW events starting in EN/LN/N instead of days does not change the conclusions (not shown). A clear spatial  
 285 modulation of MHWs by ENSO emerges. During EN, MHWs are more frequent in the northeast region—from the Society  
 286 and northern Tuamotu to the Marquesas—where up to 70% of MHW days occur during EN (Fig. 3d). In contrast, MHWs are  
 287 less common in the Austral islands during EN, accounting for only 5% of MHW days (Fig. 3d). During LN, the spatial  
 288 distribution of MHW shifts southwestward, with ~60% of MHW days in the Austral islands occurring during this phase (Fig.



289 3d). In the central region, where MHWs mostly occur during N periods (Fig. 3b), EN still enhances MHW occurrence over  
 290 the Society and Tuamotu archipelagos (Fig. 3d). For the Gambier Islands, EN and LN show no significant effects (Fig. 3d).  
 291 Figure 3e shows the ENSO phase associated with the start time of the most severe MHW (in terms of S, cf. section 2.2) at  
 292 each grid point, which closely aligns with the spatial modulation patterns described above. The most intense MHWs in the  
 293 northeastern region (north and east Tuamotu and Marquesas) tend to occur during EN, while those in the southwestern  
 294 region (Austral and south Tuamotu) are mostly associated with LN. In the central region (Society, west Tuamotu, Gambier),  
 295 the signal is more variable, but the most severe events are triggered during neutral phases.



297  
 298 **Figure 3.** Proportion of MHWs occurring during different ENSO phases: El Niño (panel a), Neutral (panel b), and La Niña (panel c).  
 299 Panel d shows the average percentage of MHWs associated with each ENSO phase for the five archipelagos of FP. The horizontal dashed  
 300 lines indicate the proportion of El Niño (red), La Niña (blue), and Neutral (gray) days over the study period (1981–2024). Comparing the  
 301 bars with the same-colored dashed lines—showing the fraction of El Niño/La Niña/Neutral days in that period—reveals how strongly  
 302 ENSO modulates MHW occurrence. Panel e shows the ENSO phase associated to the start time of the most severe MHW at each grid  
 303 point (defined following the categories of Hobday et al., 2018, cf. Methods). SST has been detrended prior to MHW detection for this  
 304 analysis (similar results were obtained without removing the trend, not shown). The same figure for austral and boreal summer MHWs  
 305 separately is shown in SI, Fig. S8-S9. Also, similar modulation is obtained by detecting MHWs in GLORYS over the same period (not  
 306 shown).



308 Similar conclusions have been obtained with MHWs detected without having removed the trend in OISST as well as with  
 309 MHWs detected in GLORYS over the same period (not shown). As shown in SI (Fig. S8 and S9), the MHW spatial patterns  
 310 modulated by ENSO revealed in Fig. 3 are exacerbated during austral summer (NDJFMA) during the peak of ENSO events  
 311 but weakened during austral winter (MJJASO). We therefore focus on the austral summer season for a more in-depth  
 312 analysis that includes ENSO diversity.

#### 313 **4.2- Modulation of MHWs by the diverse flavors of ENSO**

314 There is an important diversity of ENSO impacts during austral summer over FP especially in terms of SST intensities and  
 315 spatial patterns (Pagli et al., 2025a and Fig. 4a). Figure 4 recalls the six ENSO clusters defined by Pagli et al. (2025a,b) at  
 316 the FP scale (cf. section 2.2 and Table S1). NDJFMA composites (average across years of each cluster) of SST anomalies at  
 317 the Pacific scale (in °C) and local scale (expressed in terms of S index) are shown in panels a and b, respectively. The  
 318 composite of the percentage of days where  $S \geq 1$  is shown in panel c. Figure 5 highlights how the different ENSO flavors  
 319 impact cumulative heat stress over the warm season at the FP scale, as depicted by DHW that takes into account the time  
 320 integration of the heat stress and is recognized as an indicator of coral bleaching. The maximum of DHW reached for each  
 321 austral summer averaged over years from each ENSO clusters is displayed in Fig. 5a and the same quantity averaged over  
 322 each archipelago and for each year of the period is displayed in Fig. 5b-f. In SI (Fig. S10), MHW intensity, duration, and the  
 323 number of MHW days composited for each ENSO cluster are displayed.

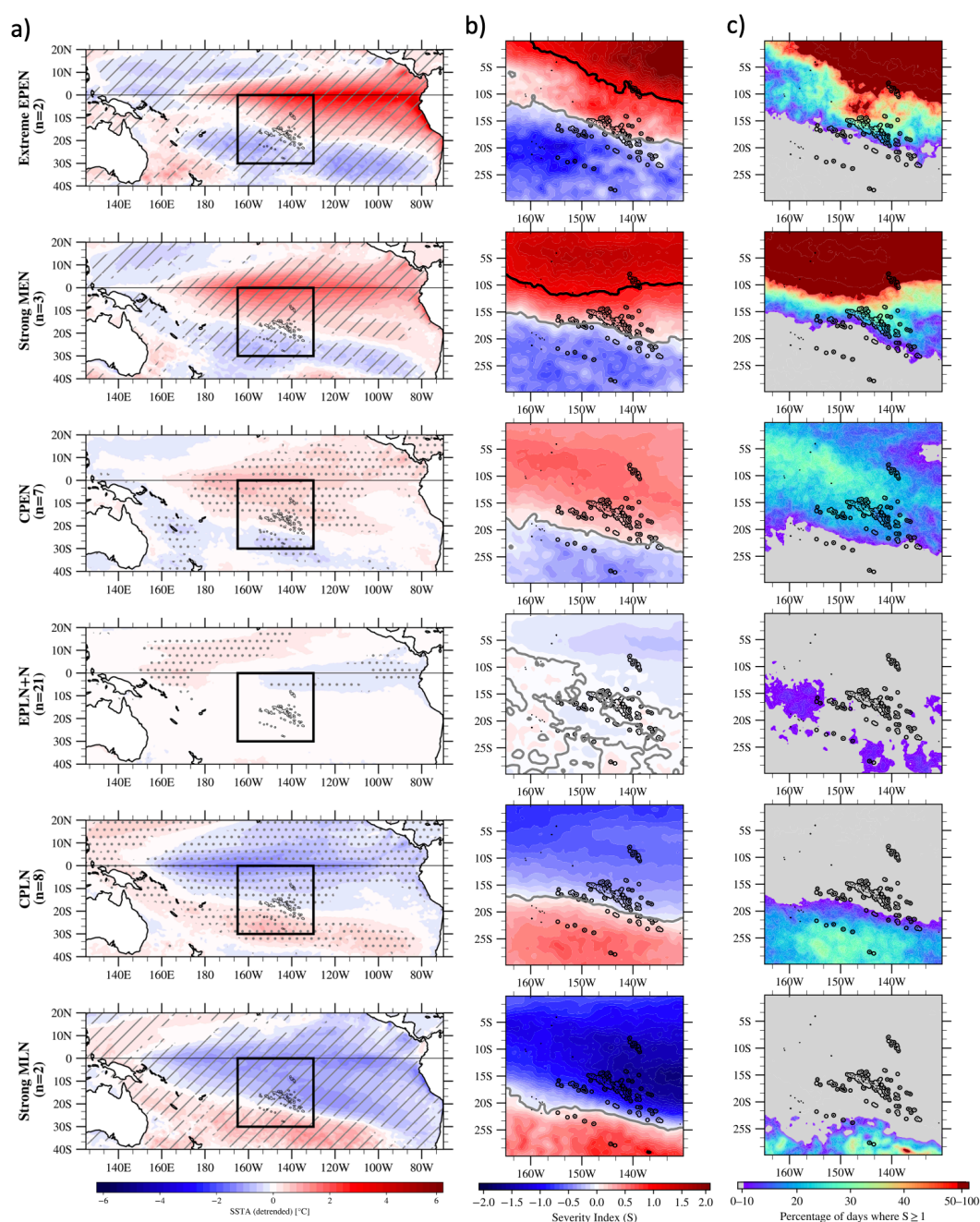
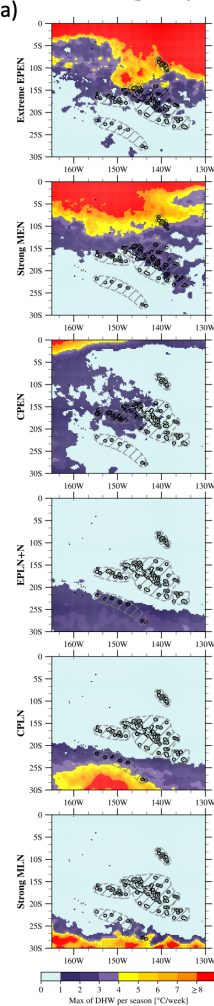


**Figure 4.** Composites of SST anomalies (linearly detrended) averaged over NDJFMA for the ENSO classification of Pagli et al., (2025a,b) at the Pacific scale (a). Cluster composites of S for NDJFMA are shown in the panel b, with isolines corresponding to  $S = 0$  and  $S = 1$  displayed in gray and black, respectively. The cluster composites of the percentage of days where  $S \geq 1$  over NDJFMA is shown on panel c. Gray (dark red) area corresponds to regions where 0 to 10% (50-100%) of the NDJFMA days satisfy this criteria. In panel a, dots indicate anomalies significant at the 90% confidence level based on a two-tailed Student t-test. The number of years ( $n$ ) in each ENSO cluster is indicated on the y-axis of panel a. For clusters spanning two or three years, gray hatching marks regions where anomalies share the same sign across all years in the cluster.

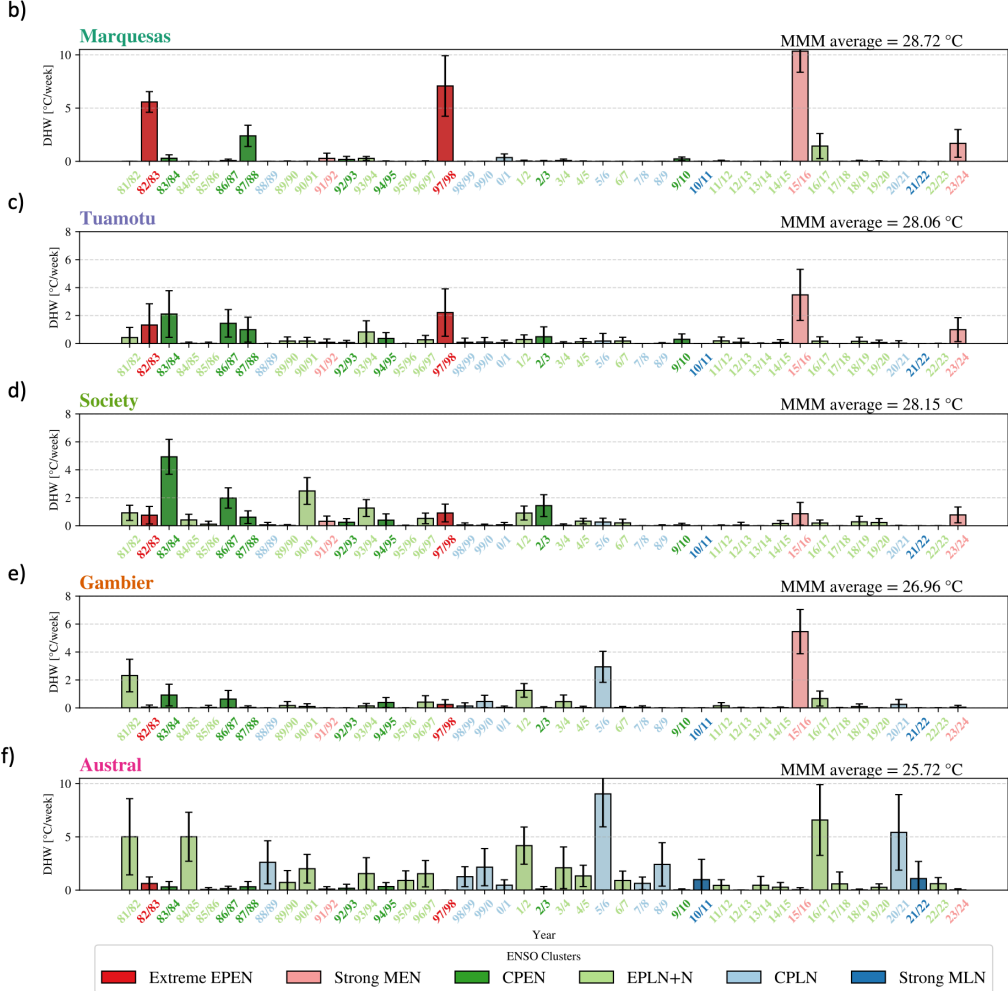


332

**Max of DHW by Warm  
Season averaged by cluster**



**Max of DHW by Warm Season averaged by Region**



333

334 **Figure 5.** ENSO cluster composites of the maximum of DHW over the warm season (a) and yearly maximum of DHW averaged over each  
335 archipelago region (b-f). For each archipelago, the spatial average of the MMM used to compute the DHW is indicated on the top right of  
336 panels b-f. Year labels on x-axis and bars are colored by ENSO cluster. The black error bars show  $\pm 1$  standard deviation across all pixels  
337 within each archipelago area. These results were computed using detrended SST data; for DHW values based on non-detrended SST data,  
338 see Fig. S11.

339

340 Figure 4 refines the ENSO modulation of MHWs during the warm season, as introduced in section 4.1 (Fig. 3). On average  
341 over the austral summer, during strong EN events, classified in strong Mixed EN (MEN) and extreme Eastern Pacific EN  
342 (EPEN) clusters, the Marquesas region and equatorward areas remain in a MHW state throughout the entire summer (90–  
343 100% of MHW days, and  $S \geq 1$  on average over the 6 months; see Fig. 4b,c). These MHWs are very long and intense (Fig.





344 S10b,c), resulting in exceptionally strong cumulative heat stress over this region (Fig. 5a). Further south, MHWs are favored  
 345 ( $0 < S < 1$ ) in a band extending from the Marquesas to northern Tuamotu and Society Islands only (Fig. 4b,c). Over this  
 346 MHW-favored area, the proportion of days with  $S \geq 1$  during the warm season increases gradually from south (10%) to north  
 347 (50%). In contrast no MHWs are detected in the far southern regions during strong MEN and extreme EPEN events. During  
 348 Central Pacific EN (CPEN), all archipelagos—except the Austral Islands—experience SSTs warmer than usual (Fig. 4a),  
 349 though still below the MHW threshold on average over the austral summer (Fig. 4b). These warmer SST favor MHW  
 350 development and result in an average of ~30% MHW days during the warm season (Fig. 4c), with a slight increase of  
 351 cumulative heat stress on average for central regions (Fig. 5a). Conversely, in the southwest, S values are on average  
 352 negative (Fig. 4), indicating unfavorable conditions for MHWs. During neutral years to weak LN (EPLN+N), S anomalies  
 353 across FP are weak and close to zero, only a few MHWs occur during some of these years over this region. During Central  
 354 Pacific LN (CPLN-englobing most of the LN events), MHWs are favored in the southern Society Islands, extreme south  
 355 Tuamotu, and the Gambier Islands, with around 20–30% of MHW days over the warm season. MHWs are generally  
 356 unfavored elsewhere. This leads to an increase of cumulative heat stress in the Austral Islands (Fig. 5a). Finally, during  
 357 strong Mixed LN (MLN) events, MHWs are favored exclusively in the extreme south of the Austral Islands (i.e., Rapa Iti),  
 358 where they are associated with strong cumulative heat stress, while unfavorable conditions prevail across the rest of FP (Fig.  
 359 5a).

360 Periods of increased cumulative heat stress coincide spatially with positive SST anomalies associated with the ENSO  
 361 clusters. However, the magnitude of DHW can vary from year to year even for similar mean SST anomalies over the season  
 362 and across archipelagos. This is because it reflects the time-integrated effect of SST anomalies and therefore the risk for  
 363 coral bleaching is not systematically reached where ENSO-related SST anomalies are positive (Fig. 5b-f). In the Marquesas,  
 364 very strong cumulative heat stress occurred during the 1982/83, 1997/98, 2015/16, and 2023/24 El Niños (extreme EPEN and  
 365 strong MEN while 1991/92 (a strong MEN) was comparatively associated with weaker cumulative intensity (Fig. 5b). We  
 366 can note also that 1987/88 (CPEN) year produced a strong heat stress over the Marquesas. In the Tuamotu, the same years in  
 367 addition to 1983/84, 1986/87 (CPEN) are linked to the highest cumulative heat stress (Fig. 5c), but with lower cumulative  
 368 heat stress than in the Marquesas. Interestingly, the 1991/92 strong MEN event, despite being extreme for FP in terms of  
 369 SPCZ displacement and tropical cyclone activity (Vincent et al., 2011; Pagli et al., 2025a,b), was not as intense in terms of  
 370 MHWs over the Marquesas and Tuamotu. In the Society archipelago, 1983/84, 2009/10, 2002/03 (CPEN) and neutral years  
 371 1990/91, 2016/17 (EPLN+N) correspond to the strongest DHW values (Fig. 5d). While strong MEN and extreme EPEN  
 372 years also produce considerable cumulative intensities in this region, they are not the highest, highlighting that the strongest  
 373 EN events (as defined on a global scale) do not always correspond to the most severe impacts over FP. In the Gambier  
 374 Islands, both EN and LN events can produce significant cumulative heat stress (2005/06 CPLN and 2015/16 strong MEN)  
 375 during the warm season (Fig. 5e), with no consistent influence of specific ENSO clusters on the cumulative heat stress. This  
 376 aligns with the unclear ENSO modulation highlighted for the Gambier Islands in Fig. 3. In the Austral Islands, the strongest  
 377 cumulative heat stress are observed in 1988/89, 2005/06 and 2020/21 LN years, particularly CPLN events.





These conclusions were drawn from analyses based on detrended SST data, aiming to isolate the ENSO imprint on cumulative heat stress over FP. However, when using the non-detrended SST data—which reflects the total heat stress exposure experienced in surface—the maximum DHW values over the warm season for years occurring after 2000 are amplified over the Tuamotu, Society, and Gambier archipelagos (Fig. S11) especially in 2015/16 (strong MEN) that has been associated with massive wide coral bleaching over FP (Hédouin et al., 2020) and more recently in 2023/24 (strong MEN).

## 5- Physical mechanisms generating and dissipating MHWs over 1993-2020

### 5.1- MHW development

In this section we investigate the physical mechanisms of the MHWs in the GLORYS oceanic reanalysis (over the 1993-2020 period, see Methods in section 2.2). We examined the dominant local mechanisms of MHWs development across the territory for austral summer and winter separately (Fig. 6) — focusing on air-sea surface heat fluxes, horizontal advection, and residual terms (see Eq. 2). The residual term consists firstly of the vertical/horizontal mixing and entrainment at the bottom of the mixed layer plus implicit heat sources/losses due to the assimilation in GLORYS (see Eq. 3). Also, because the vertical mixing may be poorly represented in GLORYS (due to the lack of explicit tidal forcing) and because the magnitude of the data-assimilation increments is unknown here, interpreting in detail this residual is beyond the scope of this study.

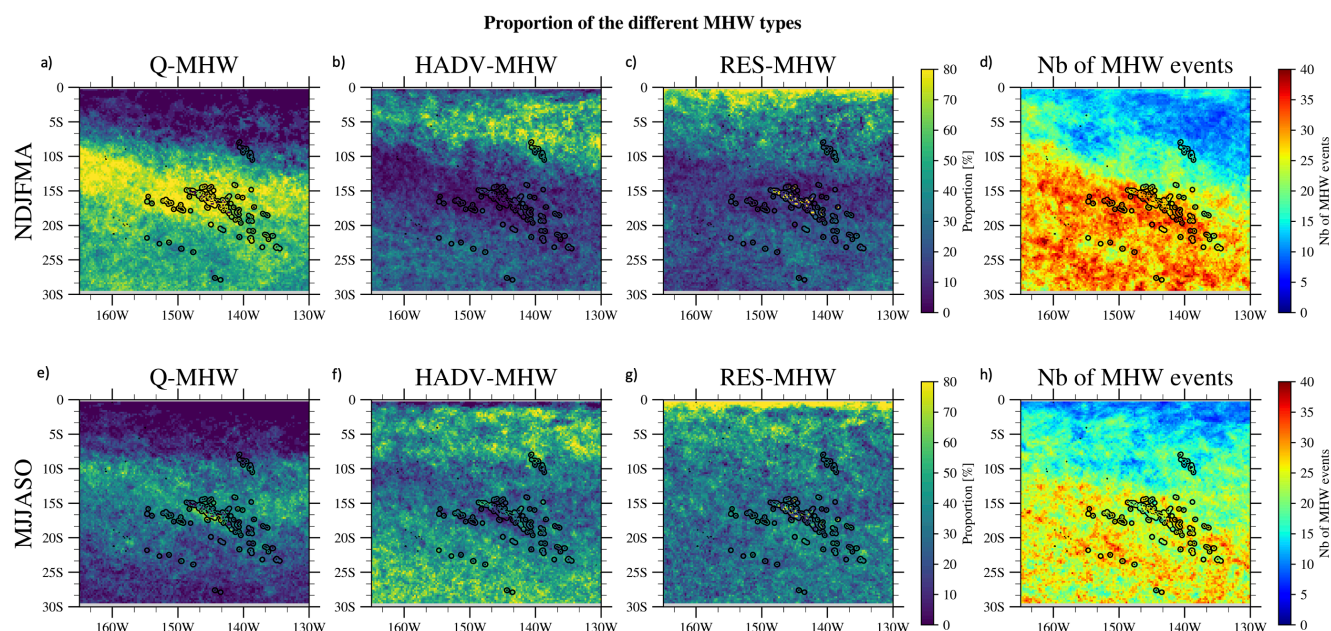


**Figure 6.** Proportion of the different MHW types for all events detected in austral summer and austral winter separately (d,h) in GLORYS, during the 1993-2020 period. Panels a and e show the proportion of Q-MHWs in austral summer and winter, respectively; panels b and f show HADV-MHWs; panels c and g show RES-MHWs. Mixed events are not shown, as they represent only a small number of cases.



397 MHWs are driven by different mechanisms depending on the region and the season (Fig. 6), and a strong differentiation  
 398 appears at about 10°S. During austral summer, MHWs are primarily flux-driven in most archipelagos south of 10°S,  
 399 especially in the central regions (Society and central Tuamotu), accounting for 70–80% of total events (Fig. 6a). HADV-  
 400 MHWs and RES-MHWs represent 0 to 30% of the total events except for MHWs occurring in the equatorward region, north  
 401 of 5°S/10°S (Fig. 6b,c). Here, HADV-MHWs dominate and account for 60-70% of the events south of 2°S. The residual (the  
 402 vertical terms and heat increments due to data assimilation) becomes dominant in a thin equatorial band due to the particular  
 403 dynamics of the region with notably the equatorial upwelling (e.g. Deppenmeier et al., 2021). During austral winter, the  
 404 proportion between MHWs types is more balanced in central regions with a slight dominance of Q-MHWs compared to  
 405 HADV-MHWs and RES-MHWs (Fig. 6e,f,g). HADV-MHWs proportion increases across the southern subtropical region  
 406 (south of 20°S) compared to summer accounting for more than 60% of total events. RES-MHWs proportion slightly  
 407 increases across FP in winter compared to summer too. Following our classification criteria (cf. section 2.2), mixed-MHW  
 408 were almost never defined over both seasons (not shown).

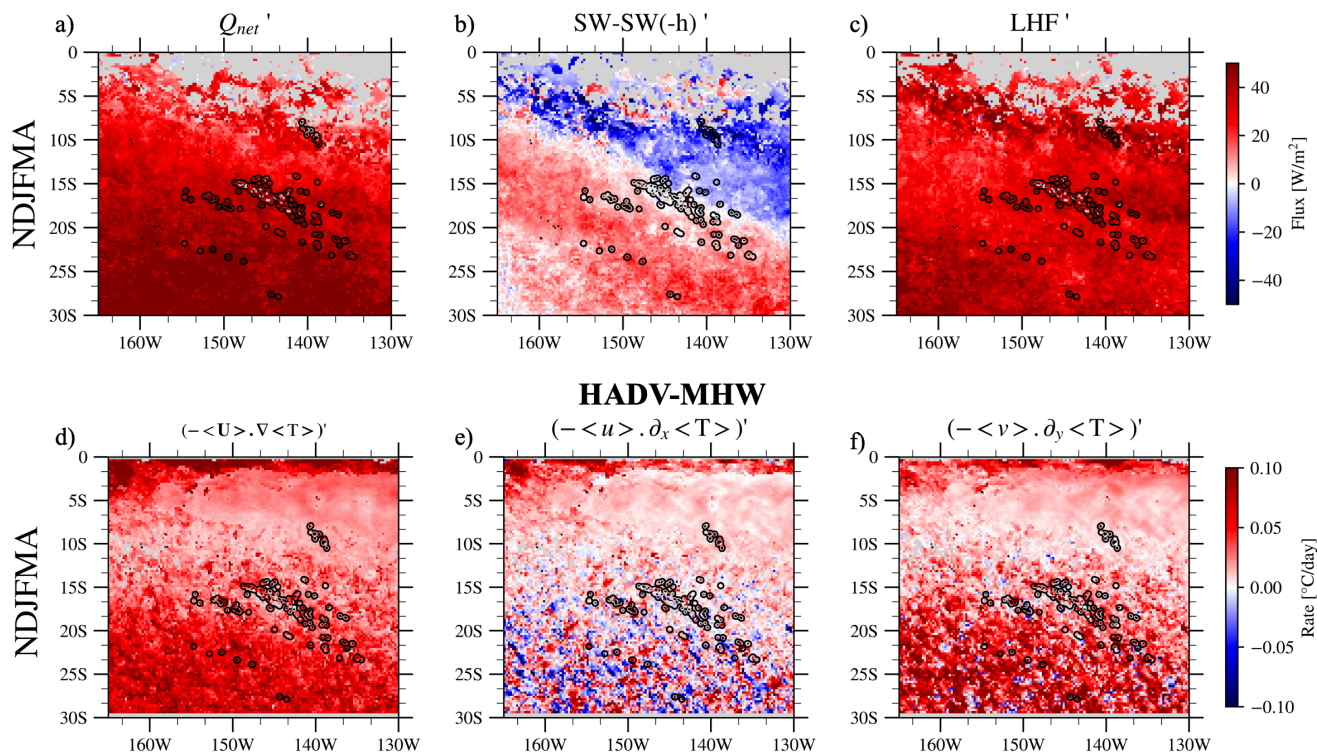
409

410 We now look at the mechanisms of MHW development for Q-MHWs and HADV-MHWs separately. For each MHW type,  
 411 the terms in Eq. (2) were averaged from start to peak at each grid point and then composited over all events for austral  
 412 summer and winter separately (Fig. A1). Only the results for the austral summer MHWs are presented in this section and  
 413 those for austral winter MHWs are available in Appendix A. The standard deviation associated to the mean composites  
 414 presented in Fig. A1 and A2 are presented respectively in Fig. S12 and S18. Because Q-MHWs are, by construction,  
 415 dominated by the air–sea heat budget term contribution, we focus on  $Q_{net}$  and its leading components, shown in Fig. 7a–c.  
 416 Conversely, since HADV-MHWs are driven by horizontal advection contribution, we focus in Fig. 7d–f on the horizontal  
 417 heat advection term and its zonal and meridional components. MLD (full field and anomalies), wind, SSH, and surface-  
 418 current anomalies are shown in Fig. 8. These results for austral winter are available in SI.



## From start to peak

### Q-MHW



419

420 **Figure 7.** Composites of the net air-sea heat flux (and its dominant components : SW-SW(-h) and LHF) for Q-MHWs and the  
 421 horizontal-advection term (and its decomposition into zonal and meridional components) for HADV-MHWs, for events peaking in the  
 422 warm season (NDJFMA), averaged over the onset-to-peak period (cf. section 2.2). Panels a–c show Q-MHW composites of (a) net air-sea  
 423 heat flux  $Q_{net}$  (b) the net shortwave flux in the mixed-layer ( $SW - SW(-h)$ ), and (c) LHF anomalies. Panels d–f show HADV-MHW  
 424 composites of (d) horizontal advection and its (e) zonal and (f) meridional components. In each panel, the composite corresponds to the  
 425 averaged across all MHWs of the corresponding type (Q-MHW or HADV-MHW) detected at each grid point.



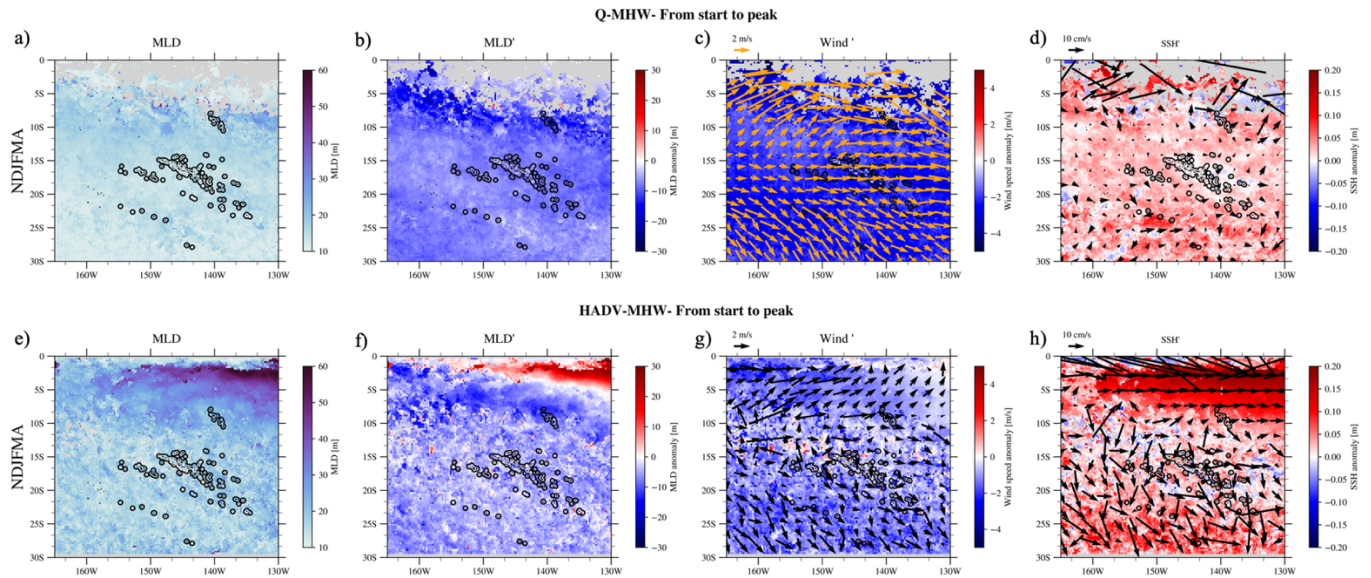


**Figure 8.** conditions from start to peak of Q-MHWs (upper panels (a–d)) and of HADV-MHWs (lower panels (e–h)). MLD (a, e), MLD anomalies (b, f), 10m-wind (speed and direction) anomalies (c, g), and SSH with oceanic currents averaged over the upper 0–30 m (d, h) for MHWs in NDJFMA. Anomalies are relative to the mean seasonal cycle computed over the whole period (1993–2020).

### Q-MHWs

The  $Q_{net}$  anomalies driving Q-MHWs development are dominated by LHF anomalies (Fig. 7a–c). Anomalously weak surface winds (Fig. 8c) reduce evaporation, thereby warming the mixed layer. The net SW anomalies in the mixed-layer play a secondary role but still modulate  $Q_{net}$  during Q-MHWs onset in summer, with a spatially complex pattern (Fig. 7b). In the northeast, where most events occur under EN, negative net SW anomalies in the mixed layer tend to damp Q-MHWs development. They are negative because incoming SW anomalies are weakly positive or negative (Fig. S13b) due to enhanced convection during EN (Pagli et al., 2025a) and thus do not offset the increased SW loss through the mixed-layer base (Fig. S13c) caused by a shoaled mixed layer under anomalously weak winds (Fig. 8b,c). In the southwest by contrast, where MHWs are favored during LN, net SW anomalies generally reinforces the warming during the onset of the event, consistent with clearer skies and enhanced incoming SW (Fig. S13a,b,c) typically seen during LN due to anomalously dry conditions over austral summer (Pagli et al., 2025a).

Although air–sea flux anomalies account for most of the variability in the  $Q_{net}/(\rho C_p h)$  term of Eq. (2), mixed-layer shoaling during onset (Fig. S15e) slightly increases the air/sea flux-term warming. In other words, a shallower mixed layer heightens its sensitivity to flux changes. Still, this effect is minor compared with the flux anomalies themselves (Fig. S15c). Horizontal advection does not exhibit a strong and systematic contribution for Q-MHWs during onset, as indicated by the noise present in HADV-MHWs composite during MHW development (Fig. A1c).



Results are broadly similar across seasons (Fig. A1e-h Fig. S14a-c, and Fig. S13d-f). During austral winter—when the seasonal mixed layer is thicker—the required LHF anomalies, and thus the wind-speed anomalies needed for Q-MHWs to develop, are larger than in austral summer (Fig. S17a,b,c). This also explains why Q-MHWs are more frequent in austral summer than in austral winter (Fig. 6a,b). Also, in winter, SW variations during MHW development are highly event-dependent with no clear pattern on the composite shown in Fig. S14b. They can either reinforce or damp the warming associated to reduced evaporation (Fig. S14a,b,c).

453

#### 454 **HADV-MHWs**

North of  $10^\circ$  S (but south of  $3^\circ$ S, out of the equatorial wave guide)—where most HADV-MHWs occur during EN (cf. Fig. 3 and 4)—both zonal and meridional heat advection contribute (Fig. 7d,e,f). The warming during the onset is associated to eastward current anomalies that transport the climatologically warmer waters from the west (Fig. 8h,  $u' \cdot \partial_x \bar{T}$  in the  $\mathbf{U}' \cdot \nabla \bar{T}$  term, Fig. S16g, h). In addition, the EN-enhanced SST gradient is advected by the mean circulation to higher latitudes, fueling HADV-MHWs' onset south of  $10^\circ$  S and up to  $20^\circ$ S ( $\bar{\mathbf{U}} \cdot \nabla T'$  term, Fig. S16d,e,f).

Moving southward, the signal becomes noisier, but meridional advection shows the most systematic warming during the development stage (Fig. 7f). This arises from persistent southeastward anomalous currents that can be forced directly by wind anomalies (Fig. 8g, h) and/or from geostrophic adjustment and/or from anomalous circulation linked to westward-propagating anticyclonic eddies (positive SSH, Fig. 8h; the composite method, done for MHWs at each grid point separately, smooth out eddies pattern, with only their SSH contribution to the MHW at the grid point being visible), which likely also contribute to the noise seen in Fig. 8h.

Air-sea flux contributions during HADV-MHWs are less systematic as shown by the noise present in the composite in Fig. A1j, sometimes reinforcing the advective warming and sometimes damping it from one event to another. Nevertheless, in the Marquesas—where most events occur under EN—the net air/sea heat flux term tends, on average, to damp the MHW development (Fig. A1j). Southwest of the Marquesas, over other archipelagos, the air/sea flux term generally provides a slight warming, though with strong event-to-event variability (Fig. A1j). Conclusions about the onset mechanisms of HADV-MHWs are very similar in austral winter (Fig. A1m-p).

Up to now we did not comment on the role of the residual term during the onset and decay of Q- and HADV- MHWs. The residual term contribution to MHW onset composited for Q-MHWs and HADV-MHWs present a strong inter-event variability and is hardly interpretable here (Fig. A1d, h, l, p). On average, for MHWs occurring north of  $10^\circ$ S, the residual term contributes to the warming of the mixed layer during the MHW onset for both Q- and HADV-MHWs and over both seasons. This may be linked to reduced vertical mixing caused by the weaker winds and shallower MLD observed during the MHW development (Fig. 8b, c, f, g and Fig. S17b, c, f, g).

RES-MHWs constitute a substantial fraction of events over FP (Fig. 6c,g). Fig. A1q-x shows the composites of the different terms of Eq. (2) during their onset. By construction, their development is driven by the residual term which may be



dominated by vertical processes (mixing and entrainment), while contributions from air–sea fluxes and horizontal heat advection are highly variable from event to event and show no systematic pattern.

## 5.2- MHW decay

We now investigate the decay stage (peak to end) of MHWs over FP. As the classification into different MHWs types has been solely designed for the developing phase (classification criteria applied regarding the terms contribution integrated from onset to peak time, cf. section 2.2), we used all MHWs together to study the decaying stage of MHWs (after verifying that decaying mechanisms do not significantly differ between MHWs types).

In austral summer, the transition from onset to decay (Fig. 9a,d) is dominated by cooling from the air–sea heat-flux budget term of Eq. (2) (Fig. A2). It is mainly due to negative  $Q_{net}$  anomalies that are mainly explained by the anomalies of the net SW in the mixed-layer in the north and of surface LHF in the south (Fig. 9a, b, c). Over the northeastern half of FP, it is the negative incoming SW anomalies that explain the most the cooling of mixed-layer temperature while LHF' continues on average to warm but with a strong inter-events variability. In the southwestern half, it is more systematically the cooling due to negative LHF anomalies i.e. increased evaporation that causes the decaying of MHWs. This can be due to increases in wind speed and/or SST or to a decrease in surface moisture (a drier air mass increasing evaporation). When looking at the composite of the wind speed anomalies for the MHW decay (Fig. 9d), these are still negative, but less than during onset, meaning that MHW warm SST and/or decrease in the surface atmosphere moisture may play a role.

In austral winter, the role of SW anomalies weakens and on average MHW decay is caused mainly by negative LHF anomalies that are more systematically associated to positive or back to normal wind speed anomalies (Fig. S19), with possibly also a role of warm SST.

### All MHWs - From peak to end

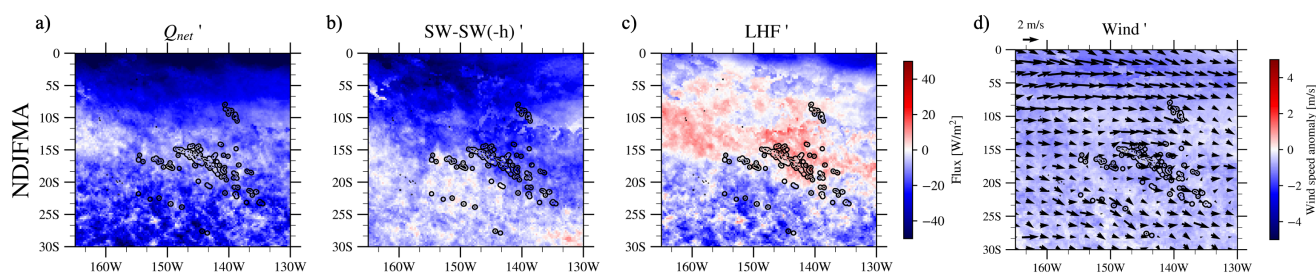


**Figure 9.** Composites of the net air–sea heat flux (and its dominant components) as well as surface wind anomalies averaged over the decay period i.e. from peak to end (cf. Methods) for all MHWs peaking in austral summer. Panels a–c show MHW composites of (a) net air–sea heat flux  $Q_{net}$  (b) the net shortwave flux in the mixed-layer ( $SW - SW(-h)$ ), and (c) LHF anomalies. In each panel, the composite is averaged across all MHWs (without distinguishing by type as done during the onset period) detected at each grid point.





During MHW decay, the residual term is more spatially coherent and exhibits less noise (Fig. A2d,h) than during the onset for Q- and HADV-MHW types (right column of Fig. A1). In austral summer, it produces anomalous warming of the mixed layer; in austral winter, it warms north of  $\sim 10^{\circ}\text{S}$  and cools south of  $\sim 15^{\circ}\text{S}$ . The nature of the residual is complex and can result from different processes. The ability of their parametrization in GLORYS to represent them and the increments of data assimilation vary in space and time. Our approach (heat budget not completely closed in a reanalysis) does not allow us to interpret more in depth this residual term. Modeling approaches capable of accurately resolving this term could enhance our understanding of the underlying processes.

### 5.3- The role of ENSO

The role of ENSO and its diversity in modulating the spatial distribution of MHWs has been highlighted in section 3.2 (Fig. 3, 4, 5). The preceding details on the mechanisms involved during the onset and decay phases of MHWs across FP further help to understand ENSO's influence. EN generates positive SST anomalies over the northeastern half of FP and negative anomalies over the southwestern half, with the opposite pattern observed during LN (Fig. 4). These SST anomalies, depending on their signs, reduce or increase the gap to the MHW threshold depending on the region, thereby creating a favorable or unfavorable background state for MHW development. Figure 10 displays surface wind, mixed layer, SSH and surface currents averaged for EN and LN separately. EN periods are characterized by a significant shoaling of the mixed layer, and reduced wind speeds across most archipelagos, therefore creating a favorable environment for MHWs development (by reducing evaporation, rendering the mixed-layer more sensitive to warming from air/sea fluxes and may also reduce the efficiency of vertical terms in cooling the mixed layer) over most regions except around Austral Islands (Fig. 10a,b). In addition to that, eastward current anomalies to the north bring warmer waters from the west and deeper thermocline over the northeastern part. Conversely, LN periods are associated with a deeper mixed layer over most regions, limiting the MHWs' development. Furthermore, LN events are associated with a deeper (shallower) thermocline to the southwest (northeast) and a shallower mixed layer and weaker winds over the Austral Islands and their southwestern margins due to the anomalous northwesterly winds (Fig. 10e). This clearly aligns with the spatial modulation of MHWs by ENSO revealed in Fig. 3. ENSO thus acts as a large-scale forcing over FP, promoting the development of MHWs in some regions while inhibiting them in others. Although a full characterization of how different ENSO flavors modulate MHW mechanisms is beyond the scope of this study, Fig. 4–5 suggest that both the spatial pattern and the amplitude of wind, mixed-layer and currents interannual anomalies likely depend on the ENSO flavor, consistent with flavor-dependent wind and precipitation anomalies (Pagli et al., 2025a). This can explain the differences observed in MHW properties and occurrences during the different EN and LN flavors (Fig. 4,5, S10).

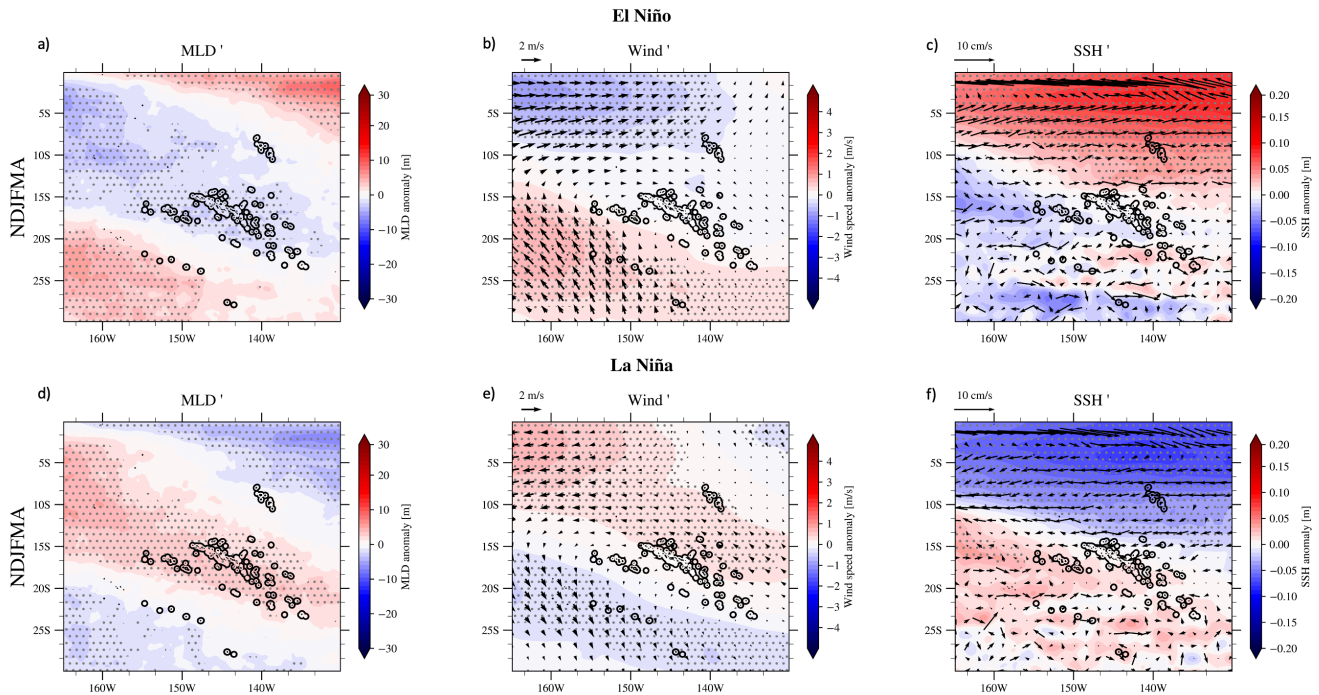


**Figure 10.** Austral summer El Niño and La Niña composites of the MLD (a,d), 10m-wind speed and direction (b,e), SSH and oceanic horizontal currents averaged from the surface to 30m (c,f) anomalies. Gray dots mark anomalies significant at the 95% confidence level (two-tailed Student t-test). The effective number of degrees of freedom have been computed as  $n \frac{(1-\rho_1)}{(1+\rho_1)} - 1$  following Bretherton et al., (1999) where  $\rho_1$  is the lag-1 autocorrelation of the each field and  $n$  is the total number of timestep (number of days here).

## 6- Conclusion

The present study provides a comprehensive assessment of MHWs in the south central Pacific across FP, characterizing their spatial and seasonal variability, mechanisms, and modulation by ENSO and its various flavors. MHWs were analyzed using OISST data for the 1981–2024 period, as well as with the GLORYS reanalysis for 1993–2024. GLORYS agreement with OISST gave us confidence in the ability of the reanalysis to study MHW mechanisms over 1993–2020. Hence, by examining the mixed layer heat budget during MHWs in GLORYS, we could determine the main mechanisms at work during MHW intensification and decay phases.

We showed that MHW occurrence, intensity, and duration vary significantly between archipelagos and seasons. The Marquesas and Austral Islands experienced the highest number of MHW days during the warm season, as well as the most intense and long-lasting events. In contrast, the Society, Tuamotu, and Gambier Islands tend to experience MHWs of lower intensity and duration, particularly during the cold season. Cumulative intensity and duration extremes also varied spatially, reflecting region-specific mechanisms.

Our results highlight the dominant role of air–sea fluxes in driving MHWs in the central regions (Society–Tuamotu–Gambier), while oceanic advection is the key mechanism generating MHWs in the Marquesas and equatorward zones up to



2°S where vertical processes dominate. In the Austral Islands and poleward zones, both air-sea fluxes and horizontal advection contribute comparably. During the cold season, the role of horizontal advection becomes more prominent across FP, while the impact of surface fluxes is dampened by a deeper seasonal mixed layer. Generally, most of MHWs decay is driven by air-sea fluxes.

We also demonstrated that ENSO exerts a strong and spatially structured modulation on MHWs in FP. EN favored MHW development in the northeastern region (Marquesas–northern Tuamotu), while LN promoted MHWs in the southwest (Austral Islands). These effects were linked to seasonally persistent changes in SST, surface wind speed, MLD, and oceanic horizontal advection patterns.

This work provides new insights into the processes controlling MHWs across FP and their connection to large-scale climate variability. It also offers a framework for understanding how future changes in ENSO behavior and ocean–atmosphere coupling might influence the frequency and severity of MHWs over the region.

## 7- Discussion

Our results regarding the classification of MHWs into different categories (Q, HADV, RES) over the South Central Pacific (Fig. 6) align with previous global modeling studies investigating dominant MHW mechanisms with mesoscale-resolving models (Marin et al., 2022, Bian et al., 2023,2024) when looking at the spatial repartition of Q-MHWs and HADV-MHWs dominated-regions. It is interesting to note that the conclusions obtained here about the mechanisms of all MHWs in FP correspond to that obtained by looking at the most extreme events (Marin et al., 2022 their Fig. 3 and 4). RES-MHWs, which are predominant in the equatorial region north of 2°S, have been mainly attributed to anomalous vertical mixing processes that warm the mixed layer during the onset and decay phases (Bian et al., 2023). Further south, over FP, the residual contributions observed during onset and decay in our analysis (Fig. A1, A2) have not been explored in detail in this study because the amplitude of the data assimilation increments is unknown. Nevertheless, as stated in our study this residual may partly reflect the effect of weakened winds during MHW onset and decay (Fig. 9) that are favored by EN (in the northeast) and LN (in the southwest), which can reduce vertical heat transfer through diffusion and local mixing (Vogt et al., 2022). It has also been shown that mesoscale eddies can inhibit the vertical mixing driven by internal waves over the region, limiting subsurface cooling and thereby promoting the development of extreme subsurface temperatures (Wyatt et al., 2023). Tides—and therefore internal tides—are not explicitly represented in GLORYS, and FP is a major internal-tide generation region (Zaron, 2019). The substantial number of RES-MHWs detected over FP (Fig. 6c,g) therefore highlights the need for regional modeling that resolves tidal processes. A regional ocean model such as the Coastal and Regional Ocean Community model (CROCO, Auclair et al., 2025), with explicit tidal forcing, would help better quantifying the residual contributions to MHWs development and decay.

One limitation of our study is the focus on SST, whereas extreme temperatures can also occur throughout the water column and cause severe impacts on ecosystems (Wyatt et al., 2023) — either synchronously with the surface, more intense, less



intense, or even entirely decoupled from surface extremes (Zhang et al., 2023). The mechanisms driving these subsurface extremes may differ from those at the surface revealed in this work, due to the vertical structure of ocean currents in the region and the progressive attenuation of air–sea flux influences with depth. Our analysis gives confidence in GLORYS, to study vertical extent of MHW. Lal et al. (2025) showed that surface MHWs in the extreme western part of FP are generally confined to the seasonal mixed layer north of 20°S, but extend deeper south of this latitude, providing an indication of what might be expected for the vertical extent of MHWs detected over FP in this study.

We showed that ENSO provided favorable or unfavorable background conditions for MHW development during the warm season and to a lesser extent over the austral winter, depending on the region within FP and the ENSO phase. However, except in the extreme northern regions, including the Marquesas during extreme EPEN and strong MEN events—where the surface ocean remains in a persistent MHW state throughout the whole warm season—the actual triggers of the mechanisms creating MHW onset (extreme LHF and SW anomalies) remain to be fully understood. Intra-seasonal processes such as the Madden–Julian Oscillation (MJO), equatorial wave activity, and/or stochastic weather/oceanic events (TCs, prolonged periods of high/ weak surface winds, prolonged precipitation/clear sky periods, SPCZ intra-seasonal, variability, oceanic eddies) may initiate or terminate MHWs. In this context, ENSO primarily modulated the background state, influencing how these intra-seasonal triggers affect MHW development and persistence (MJO-ENSO compound events as an example, Dutheil et al., 2024). Further work is needed to understand how ENSO and these higher frequency variations interact together.

Our work builds on ongoing efforts to understand the characteristics and mechanisms of MHWs across South Pacific countries (Dutheil et al., 2024; Lal et al., 2025). MHWs display distinct features between the western and central South Pacific, underscoring the need for such regional analyses. Even within the FP region, while we present results at the archipelago scale, notable variability has been found within the Tuamotu archipelago itself, which spans from about 10°N to 23°S (Fig. 3e).

Many of the FP islands (except in the Marquesas) are fringed by reefs that enclose lagoons, which most of the time represent a key economic resource for local communities. MHWs can have devastating impacts on such ecosystems (Glynn, 1984; Mumby et al., 2001b; Andréfouët et al., 2015; Andréfouët and Adjeroud, 2019; Hédouin et al., 2020). These lagoons exhibit diverse geomorphological characteristics, such as differences in size and degree of openness to the open ocean, making it challenging to assess how large-scale oceanic MHWs propagate into these more sheltered environments. To achieve this at the atoll and lagoon scale, this requires validating high-resolution satellite SST products against in-situ observations (e.g., ReefTemp; Van Wynsberge et al., 2017; Le Gendre et al., 2024), alongside a detailed understanding of lagoon hydrodynamics (Bruyère et al., 2023). Additionally, the development of statistical models that relate lagoon interior surface temperatures to oceanic temperatures and ocean–meteorological conditions could help compensate for the current lack of high-resolution SST data (Van Wynsberge et al., 2017, 2024).

In Fig. 5 we related ENSO flavors to DHW, the NOAA metric used to monitor coral bleaching globally. NOAA’s historical alert levels are: 0–4 (possible bleaching), 4–8 (reef-wide bleaching risk), and >8 (reef-wide bleaching with potential



mortality). In our record, the 8 threshold is rarely reached in the Society and Tuamotu—even in 2015/16 (Fig. 5; Fig. S11), when widespread bleaching was documented (Hédouin et al., 2020). This underscores known limitations of the standard DHW formulation, which can underpredict bleaching and overlooks regional sensitivities. It has been shown that tuning the hotspot definition, accumulation window, and/or bleaching threshold improves coral bleaching forecast skill (e.g. Lachs et al., 2021; Whitaker and DeCarlo, 2024). Accordingly, Fig. 5 quantitative results should not be read directly as relating the presence of coral bleaching; rather, it shows how ENSO modulates cumulative heat stress across FP’s archipelagos. Bleaching occurrence is also modulated by other environmental factors than heat stress—e.g., the shortwave radiation reaching colonies, salinity, water depth, nutrient supply, and local hydrodynamics (DeCarlo et al., 2020; Gonzalez-Espinosa and Donner, 2021). As an example, over FP increased cloud cover has been suspected to spread Society Islands from massive coral bleaching in the extreme EPEN 1997/98 event (Mumby et al., 2001).

While OISST dataset has been shown to be well-suited for the analysis carried out in this study Gupta and Sil (2024), differences between SST products can be significant for some MHWs commonly used metrics and this should be kept in mind. For analyzing ENSO modulation, products generally yield consistent patterns (here OISST and GLORYS are coherent). However, at the archipelago scale, quantitative metrics can differ between products (Fig. S7).

Our results provide crucial insights into the mechanisms driving MHWs over FP and their link with ENSO, which are essential for improving seasonal-to-interannual forecasts of these extreme events. The forecasting skill of MHWs varies significantly depending on season, region, and lead time (de Boissésou and Balmaseda, 2024; Cohen et al., 2025; Jacox et al., 2022). In particular, there is a strong ENSO imprint on the predictability of these events. Over the northeastern region of FP, MHWs appear much more predictable than in southern regions, with minimal forecast skill in the central areas where MHWs are primarily controlled by air–sea fluxes (Fig. 6). In the southwestern part of FP, MHW forecast skill is also weak, likely due to the dominant influence of horizontal advection (HADV) and mesoscale circulation features during the MHW onset and decay. These findings point to the need for higher-resolution models, along with an expanded network of ocean observations, to improve verification of the models and forecasting capabilities in this region.

Across the entire FP region, both the number of MHW days and event durations have increased over time (Fig. S20). However, maximum intensity has increased only in the southwestern half of the country—including the Society Archipelago, southern Tuamotu, Gambier, and Austral Islands—while the northern Tuamotu and Marquesas have experienced a decrease in maximum MHW intensity over time (Fig. S20b). The spatial pattern of this trend closely mirrors that of the long-term SST trend across the region (see Fig. S1). The underlying cause of this cooling trend in the northeast which extends more broadly in the eastern tropical Pacific remains to be clarified—whether it reflects the influence of global warming, natural tropical Pacific decadal variability, or more likely a combination of both (Watanabe et al., 2024). Therefore, the observed cooling trend in MHWs intensity over the northeastern region needs to be interpreted carefully.



656 *Authors contribution*

657 BP, TI and SC designed the study and wrote the initial manuscript draft. BP performed the analysis presented in this  
658 manuscript. Discussions and iterative feedback from all co-authors significantly contributed to the revision of the  
659 manuscript.

660

661 *Competing interests*

662 The authors declare that they have no conflict of interest.

663

664 *Acknowledgments*

665 B. P. is supported by the Institut de Recherche pour le Développement (IRD) through IRD PhD funding and is hosted at the  
666 UMR 241 SECOPOL laboratory at UPF. The author acknowledge the support of the French Agence Nationale de la  
667 Recherche (ANR), as part of the France 2030 program, under grant ANR-23-POCE-0001 (project MaHeWa), and of the  
668 Fonds Pacifique (project HEAT). We acknowledge the use of Python and NOAA Pyfer- ret languages and of the several data  
669 servers listed below.

670

671 *Data Availability Statement*

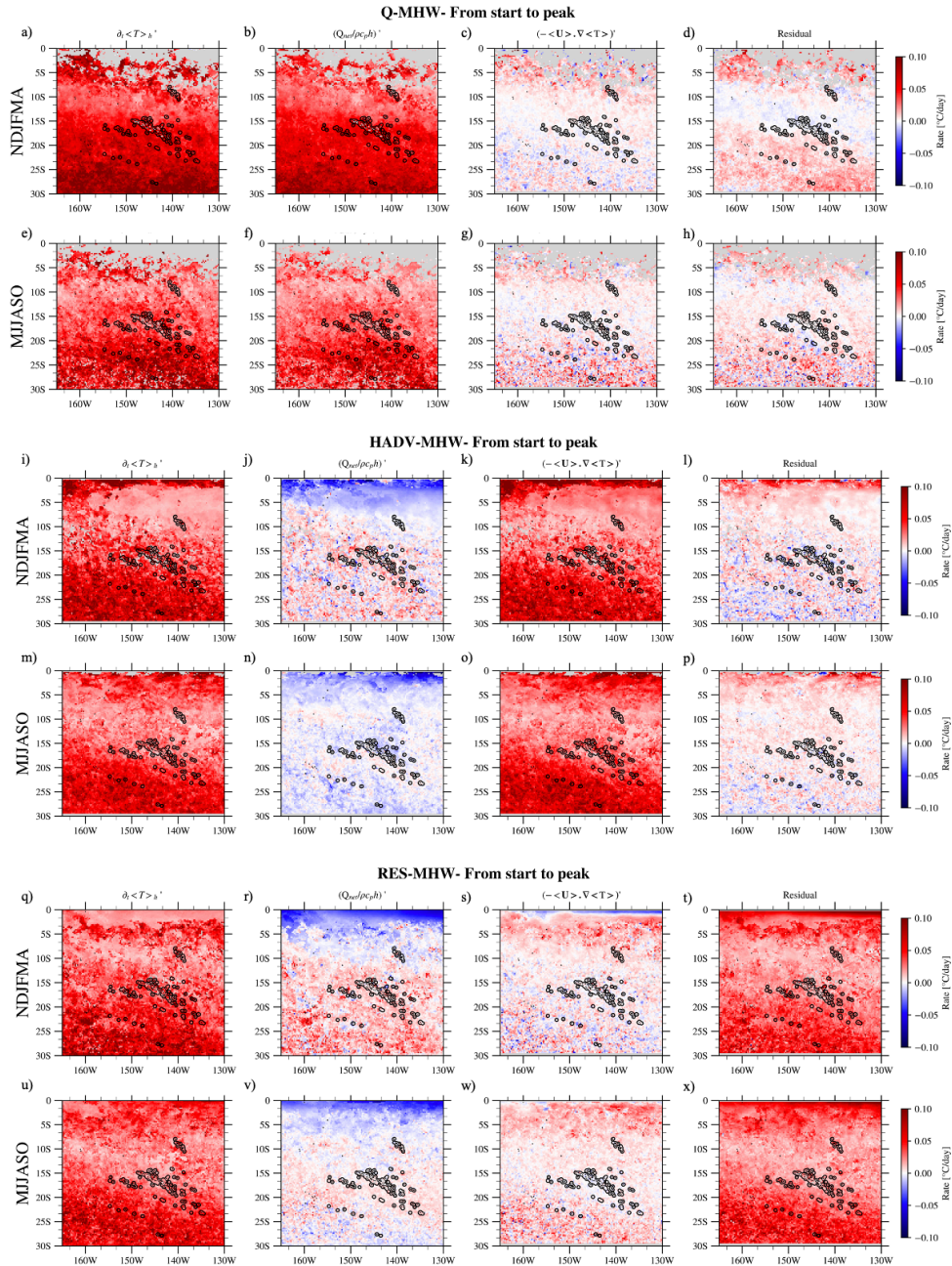
672 All datasets used in this study are open source and available online. The OISSTv2 data were downloaded from  
673 <https://psl.noaa.gov/data/gridded/data.noaa.oisst.v2.highres.html>. The GLORYS reanalysis is available on Copernicus  
674 [https://data.marine.copernicus.eu/product/GLOBAL\\_MULTIYEAR\\_PHY\\_001\\_030/description](https://data.marine.copernicus.eu/product/GLOBAL_MULTIYEAR_PHY_001_030/description). All scripts used to obtain the  
675 results presented in this study were written in Python and Pyferret and can be shared upon request.

676





## 677 APPENDIX A



678  
 679 **Figure A1.** Composites across all events at each grid point of the different term of the heat budget analysis Eq. (2) averaged from start to  
 680 peak for each MHW type and for each season separately. The first column corresponds to the mixed-layer temperature tendency term, the  
 681 second one corresponds to air/sea flux heat budget term, the third one corresponds to the horizontal heat advection term and the fourth one  
 682 corresponds to the residual term. They are all expressed in °C/day. Panels a–d and e–h show composites of Q-MHWs during austral  
 683 summer and winter, respectively. Panels i–l and m–p show composites of HADV-MHWs for summer and winter, respectively. Panels q–t  
 684 and u–x present composites of RES-MHWs in austral summer and winter, respectively.

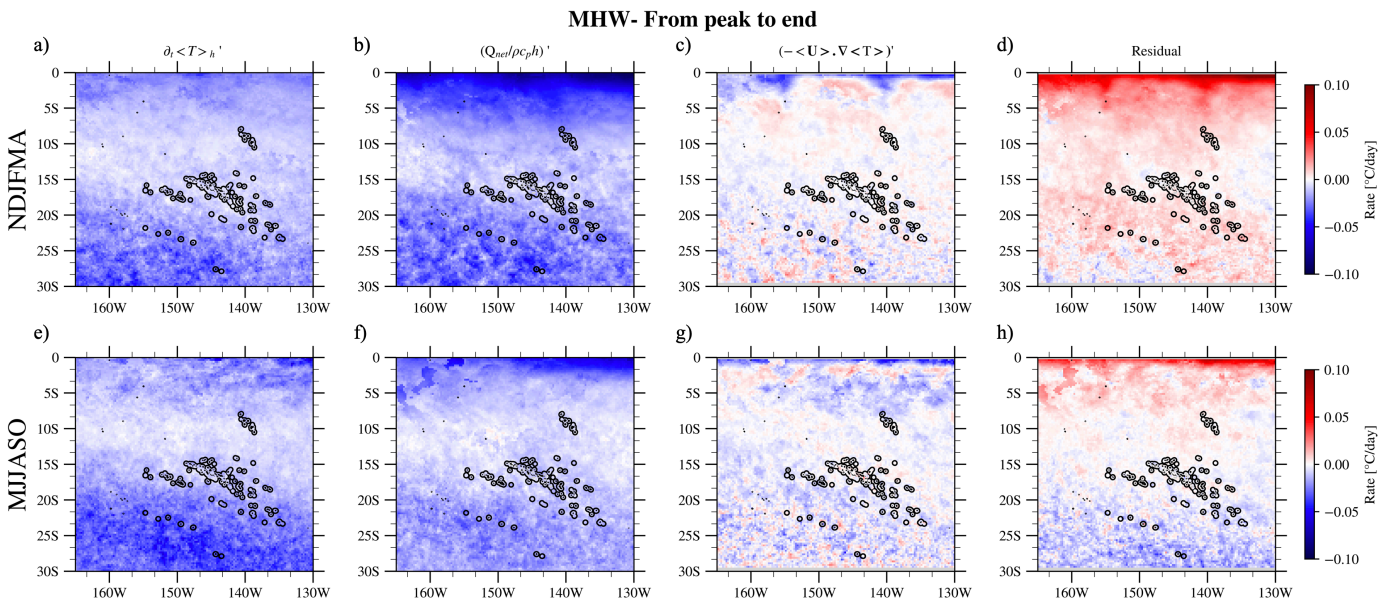


**Figure A2.** Composites across all events at each grid point of the different term of the heat budget analysis Eq. (2) averaged from peak to end for all MHWs and for each season separately. The first column corresponds to the mixed-layer temperature tendency term, the second one corresponds to air/sea flux heat budget term, the third one corresponds to the horizontal heat advection term and the fourth one corresponds to the residual term. They are all expressed in °C/day. Panels a-d and e-h show the composite over MHWs in austral summer and winter respectively.

## References

- Amaya, D. J., Jacox, M. G., Fewings, M. R., Saba, V. S., Stuecker, M. F., Rykaczewski, R. R., Ross, A. C., Stock, C. A., Capotondi, A., Petrik, C. M., Bograd, S. J., Alexander, M. A., Cheng, W., Hermann, A. J., Kearney, K. A., and Powell, B. S.: Marine heatwaves need clear definitions so coastal communities can adapt, *Nature*, 616, 29–32, <https://doi.org/10.1038/d41586-023-00924-2>, 2023.
- Andréfouët, S. and Adjeroud, M.: French Polynesia, in: *World Seas: an Environmental Evaluation*, Elsevier, 827–854, <https://doi.org/10.1016/B978-0-08-100853-9.00039-7>, 2019.
- Andréfouët, S., Dutheil, C., Menkes, C. E., Bador, M., and Lengaigne, M.: Mass mortality events in atoll lagoons: environmental control and increased future vulnerability, *Glob. Change Biol.*, 21, 195–205, <https://doi.org/10.1111/gcb.12699>, 2015.
- Auclair, F., Benshila, R., Bordoio, L., Boutet, M., Brémond, M., Caillaud, M., Cambon, G., Capet, X., Debreu, L., Ducousso, N., Dufois, F., Dumas, F., Ethé, C., Gula, J., Hourdin, C., Illig, S., Jullien, S., Corre, M. L., Gac, S. L., Gentil, S. L., Lemarié, F., Marchesiello, P., Mazoyer, C., Morvan, G., Nguyen, C., Penven, P., Person, R., Pianezze, J., Pous, S., Renault, L., Roblou, L., Sepulveda, A., Theetten, S., Schaefer, A.-L., Treillou, S., and Valat, S.: Coastal and Regional Ocean COMmunity model, <https://doi.org/10.5281/zenodo.15064113>, 2025.



- 707 Bian, C., Jing, Z., Wang, H., Wu, L., Chen, Z., Gan, B., and Yang, H.: Oceanic mesoscale eddies as crucial drivers of global  
 708 marine heatwaves, *Nat. Commun.*, 14, 2970, <https://doi.org/10.1038/s41467-023-38811-z>, 2023.
- 709 Bian, C., Jing, Z., Wang, H., and Wu, L.: Scale-Dependent Drivers of Marine Heatwaves Globally, *Geophys. Res. Lett.*, 51,  
 710 e2023GL107306, <https://doi.org/10.1029/2023GL107306>, 2024.
- 711 de Boissésou, E. and Balmaseda, M. A.: Predictability of marine heatwaves: assessment based on the ECMWF seasonal  
 712 forecast system, *Ocean Sci.*, 20, 265–278, <https://doi.org/10.5194/os-20-265-2024>, 2024.
- 713 Bretherton, C. S., Widmann, M., Dymnikov, V. P., Wallace, J. M., and Bladé, I.: The Effective Number of Spatial Degrees  
 714 of Freedom of a Time-Varying Field, *J. Clim.*, 12, 1990–2009, [https://doi.org/10.1175/1520-0442\(1999\)012<1990:TENOSD>2.0.CO;2](https://doi.org/10.1175/1520-0442(1999)012<1990:TENOSD>2.0.CO;2), 1999.
- 716 Bruyère, O., Le Gendre, R., Chauveau, M., Bourgeois, B., Varillon, D., Butscher, J., Trophime, T., Follin, Y., Aucan, J.,  
 717 Liao, V., and Andréfouët, S.: Lagoon hydrodynamics of pearl farming atolls: the case of Raroia, Takapoto, Apataki and  
 718 Takaroa (French Polynesia), *Earth Syst. Sci. Data*, 15, 5553–5573, <https://doi.org/10.5194/essd-15-5553-2023>, 2023.
- 719 Capotondi, A., Wittenberg, A. T., Kug, J.-S., Takahashi, K., and McPhaden, M. J.: ENSO Diversity, in: *El Niño Southern*  
 720 *Oscillation in a Changing Climate*, American Geophysical Union (AGU), 65–86,  
 721 <https://doi.org/10.1002/9781119548164.ch4>, 2020.
- 722 Capotondi, A., Rodrigues, R. R., Sen Gupta, A., Benthuisen, J. A., Deser, C., Frölicher, T. L., Lovenduski, N. S., Amaya, D.  
 723 J., Le Grix, N., Xu, T., Hermes, J., Holbrook, N. J., Martinez-Villalobos, C., Masina, S., Roxy, M. K., Schaeffer, A.,  
 724 Schlegel, R. W., Smith, K. E., and Wang, C.: A global overview of marine heatwaves in a changing climate, *Commun. Earth*  
 725 *Environ.*, 5, 701, <https://doi.org/10.1038/s43247-024-01806-9>, 2024.
- 726 Cohen, J. T., Thompson, L., Maroon, E., Deppenmeier, A.-L., and Cai, C.: Object-Based Evaluation of Seasonal-to-  
 727 Multiyear Marine Heatwave Predictions, *Geophys. Res. Lett.*, 52, e2025GL115021, <https://doi.org/10.1029/2025GL115021>,  
 728 2025.
- 729 DeCarlo, T. M., Gajdzik, L., Ellis, J., Coker, D. J., Roberts, M. B., Hammerman, N. M., Pandolfi, J. M., Monroe, A. A., and  
 730 Berumen, M. L.: Nutrient-supplying ocean currents modulate coral bleaching susceptibility, *Sci. Adv.*, 6, eabc5493,  
 731 <https://doi.org/10.1126/sciadv.abc5493>, 2020.
- 732 Dee, D. P., Uppala, S. M., Simmons, A. J., Berrisford, P., Poli, P., Kobayashi, S., Andrae, U., Balmaseda, M. A., Balsamo,  
 733 G., Bauer, P., Bechtold, P., Beljaars, A. C. M., Van De Berg, L., Bidlot, J., Bormann, N., Delsol, C., Dragani, R., Fuentes,  
 734 M., Geer, A. J., Haimberger, L., Healy, S. B., Hersbach, H., Hólm, E. V., Isaksen, I., Kållberg, P., Köhler, M., Matricardi,  
 735 M., McNally, A. P., Monge-Sanz, B. M., Morcrette, J. -J., Park, B. -K., Peubey, C., De Rosnay, P., Tavolato, C., Thépaut, J.  
 736 -N., and Vitart, F.: The ERA-Interim reanalysis: configuration and performance of the data assimilation system, *Q. J. R.*  
 737 *Meteorol. Soc.*, 137, 553–597, <https://doi.org/10.1002/qj.828>, 2011.
- 738 Deppenmeier, A.-L., Bryan, F. O., Kessler, W. S., and Thompson, L.: Modulation of Cross-Isothermal Velocities with  
 739 ENSO in the Tropical Pacific Cold Tongue, *J. Phys. Oceanogr.*, 51, 1559–1574, <https://doi.org/10.1175/JPO-D-20-0217.1>,  
 740 2021.
- 741 Dutheil, C., Lal, S., Lengaigne, M., Cravatte, S., Menkès, C., Receveur, A., Börgel, F., Gröger, M., Houllbreque, F., Le  
 742 Gendre, R., Mangolte, I., Peltier, A., and Meier, H. E. M.: The massive 2016 marine heatwave in the Southwest Pacific: An  
 743 “El Niño–Madden-Julian Oscillation” compound event, *Sci. Adv.*, 10, eadp2948, <https://doi.org/10.1126/sciadv.adp2948>,  
 744 2024.





- 745 Elzahaby, Y., Schaeffer, A., Roughan, M., and Delaux, S.: Oceanic Circulation Drives the Deepest and Longest Marine  
 746 Heatwaves in the East Australian Current System, *Geophys. Res. Lett.*, 48, e2021GL094785,  
 747 <https://doi.org/10.1029/2021GL094785>, 2021.
- 748 Elzahaby, Y., Schaeffer, A., Roughan, M., and Delaux, S.: Why the Mixed Layer Depth Matters When Diagnosing Marine  
 749 Heatwave Drivers Using a Heat Budget Approach, *Front. Clim.*, 4, <https://doi.org/10.3389/fclim.2022.838017>, 2022.
- 750 Glynn, P. W.: Widespread Coral Mortality and the 1982–83 El Niño Warming Event, *Environ. Conserv.*, 11, 133–146,  
 751 <https://doi.org/10.1017/S0376892900013825>, 1984.
- 752 Gonzalez-Espinosa, P. C. and Donner, S. D.: Cloudiness reduces the bleaching response of coral reefs exposed to heat stress,  
 753 *Glob. Change Biol.*, 27, 3474–3486, <https://doi.org/10.1111/gcb.15676>, 2021.
- 754 Gregory, C. H., Artana, C., Lama, S., León-FonFay, D., Sala, J., Xiao, F., Xu, T., Capotondi, A., Martinez-Villalobos, C.,  
 755 and Holbrook, N. J.: Global Marine Heatwaves Under Different Flavors of ENSO, *Geophys. Res. Lett.*, 51,  
 756 e2024GL110399, <https://doi.org/10.1029/2024GL110399>, 2024.
- 757 Gupta, H. and Sil, S.: Assessment of GHR SST and OISST Datasets in Identification of Marine Heat-Waves and Heat-  
 758 Spikes, *IEEE Geosci. Remote Sens. Lett.*, 21, 1–5, <https://doi.org/10.1109/LGRS.2024.3362474>, 2024.
- 759 Hédouin, L., Rouzé, H., Berthe, C., Perez-Rosales, G., Martinez, E., Chancerelle, Y., Galand, P. E., Lerouvreur, F., Nugues,  
 760 M. M., Pochon, X., Siu, G., Steneck, R., and Planes, S.: Contrasting patterns of mortality in Polynesian coral reefs following  
 761 the third global coral bleaching event in 2016, *Coral Reefs*, 39, 939–952, <https://doi.org/10.1007/s00338-020-01914-w>,  
 762 2020.
- 763 Hersbach, H., Bell, B., Berrisford, P., Hirahara, S., Horányi, A., Muñoz-Sabater, J., Nicolas, J., Peubey, C., Radu, R.,  
 764 Schepers, D., Simmons, A., Soci, C., Abdalla, S., Abellan, X., Balsamo, G., Bechtold, P., Biavati, G., Bidlot, J., Bonavita,  
 765 M., De Chiara, G., Dahlgren, P., Dee, D., Diamantakis, M., Dragani, R., Flemming, J., Forbes, R., Fuentes, M., Geer, A.,  
 766 Haimberger, L., Healy, S., Hogan, R. J., Hólm, E., Janisková, M., Keeley, S., Laloyaux, P., Lopez, P., Lupu, C., Radnoti, G.,  
 767 de Rosnay, P., Rozum, I., Vamborg, F., Villaume, S., and Thépaut, J.-N.: The ERA5 global reanalysis, *Q. J. R. Meteorol.*  
 768 *Soc.*, 146, 1999–2049, <https://doi.org/10.1002/qj.3803>, 2020.
- 769 Hobday, A. J., Alexander, L. V., Perkins, S. E., Smale, D. A., Straub, S. C., Oliver, E. C. J., Benthuisen, J. A., Burrows, M.  
 770 T., Donat, M. G., Feng, M., Holbrook, N. J., Moore, P. J., Scannell, H. A., Sen Gupta, A., and Wernberg, T.: A hierarchical  
 771 approach to defining marine heatwaves, *Prog. Oceanogr.*, 141, 227–238, <https://doi.org/10.1016/j.pocean.2015.12.014>, 2016.
- 772 Hobday, A. J., Oliver, E. C. J., Gupta, A. S., Benthuisen, J. A., Burrows, M. T., Donat, M. G., Holbrook, N. J., Moore, P. J.,  
 773 Thomsen, M. S., Wernberg, T., and Smale, D. A.: Categorizing and Naming MARINE HEATWAVES, *Oceanography*, 31,  
 774 162–173, 2018.
- 775 Holbrook, N. J., Scannell, H. A., Sen Gupta, A., Benthuisen, J. A., Feng, M., Oliver, E. C. J., Alexander, L. V., Burrows, M.  
 776 T., Donat, M. G., Hobday, A. J., Moore, P. J., Perkins-Kirkpatrick, S. E., Smale, D. A., Straub, S. C., and Wernberg, T.: A  
 777 global assessment of marine heatwaves and their drivers, *Nat. Commun.*, 10, 2624, <https://doi.org/10.1038/s41467-019-10206-z>, 2019.
- 779 Holbrook, N. J., Hernaman, V., Koshiha, S., Lako, J., Kajtar, J. B., Amosa, P., and Singh, A.: Impacts of marine heatwaves  
 780 on tropical western and central Pacific Island nations and their communities, *Glob. Planet. Change*, 208, 103680,  
 781 <https://doi.org/10.1016/j.gloplacha.2021.103680>, 2022.



- 782 Huang, B., Liu, C., Banzon, V., Freeman, E., Graham, G., Hankins, B., Smith, T., and Zhang, H.-M.: Improvements of the  
 783 Daily Optimum Interpolation Sea Surface Temperature (DOISST) Version 2.1, *J. Clim.*, 34, 2923–2939,  
 784 <https://doi.org/10.1175/JCLI-D-20-0166.1>, 2021.
- 785 Jacox, M. G., Alexander, M. A., Amaya, D., Becker, E., Bograd, S. J., Brodie, S., Hazen, E. L., Pozo Buil, M., and  
 786 Tommasi, D.: Global seasonal forecasts of marine heatwaves, *Nature*, 604, 486–490, [https://doi.org/10.1038/s41586-022-](https://doi.org/10.1038/s41586-022-04573-9)  
 787 04573-9, 2022.
- 788 Lachs, L., Bythell, J. C., East, H. K., Edwards, A. J., Mumby, P. J., Skirving, W. J., Spady, B. L., and Guest, J. R.: Fine-  
 789 Tuning Heat Stress Algorithms to Optimise Global Predictions of Mass Coral Bleaching, *Remote Sens.*, 13, 2677,  
 790 <https://doi.org/10.3390/rs13142677>, 2021.
- 791 Lal, S., Cravatte, S., Menkes, C., Macdonald, J., LeGendre, R., Mangolte, I., Dutheil, C., Holbrook, N., and Nicol, S.:  
 792 Characterization of Past Marine Heatwaves around South Pacific Island Countries: What really matters?, *EGUsphere*, 1–48,  
 793 <https://doi.org/10.5194/egusphere-2025-3281>, 2025.
- 794 Le Gendre, R., Varillon, D., Fiat, S., Hocdé, R., De Ramon N'Yeurt, A., Aucan, J., Cravatte, S., Duphil, M., Ganachaud, A.,  
 795 Gaudron, B., Kestenare, E., Liao, V., Pelletier, B., Peltier, A., Schaefer, A.-L., Trophime, T., Van Wylsberge, S.,  
 796 Dandonneau, Y., Allenbach, M., and Menkes, C.: ReefTEMPs: The Pacific Islands Coastal Temperature Network, *Earth*  
 797 *Syst. Sci. Data Discuss.*, 1–41, <https://doi.org/10.5194/essd-2024-394>, 2024.
- 798 Lellouche, J.-M., Greiner, E., Le Galloudec, O., Garric, G., Regnier, C., Drevillon, M., Benkiran, M., Testut, C.-E.,  
 799 Bourdalle-Badie, R., Gasparin, F., Hernandez, O., Levier, B., Drillet, Y., Remy, E., and Le Traon, P.-Y.: Recent updates to  
 800 the Copernicus Marine Service global ocean monitoring and forecasting real-time 1/12° high-resolution system, *Ocean Sci.*,  
 801 14, 1093–1126, <https://doi.org/10.5194/os-14-1093-2018>, 2018.
- 802 Lellouche, J.-M., Greiner, E., Bourdallé-Badie, R., Garric, G., Melet, A., Drévillon, M., Bricaud, C., Hamon, M., Le  
 803 Galloudec, O., Regnier, C., Candela, T., Testut, C.-E., Gasparin, F., Ruggiero, G., Benkiran, M., Drillet, Y., Le Traon, P.-Y.,  
 804 Bourdallé-Badie, R., Garric, G., Melet, A., Drévillon, M., Bricaud, C., Hamon, M., Le Galloudec, O., Regnier, C., Candela,  
 805 T., Testut, C.-E., Gasparin, F., Ruggiero, G., Benkiran, M., Drillet, Y., and Le Traon, P.-Y.: The Copernicus Global 1/12°  
 806 Oceanic and Sea Ice GLORYS12 Reanalysis, *Front. Earth Sci.*, 9, <https://doi.org/10.3389/feart.2021.698876>, 2021.
- 807 Madec, G., Bell, M., Benshila, R., Blaker, A., Boudrallé-Badie, R., Bricaud, C., Bruciaferri, D., Carneiro, D., Castrillo, M.,  
 808 Calvert, D., Chanut, J., Clementi, E., Coward, A., Laverne, C. de, Dobricic, S., Epicoco, I., Éthé, C., Fiedler, E., Ford, D.,  
 809 Furner, R., Ganderton, J., Graham, T., Harle, J., Hutchinson, K., Iovino, D., King, R., Lea, D., Levy, C., Lovato, T.,  
 810 Maisonnave, E., Mak, J., Sanchez, J. M. C., Martin, M., Martin, N., Martins, D., Masson, S., Mathiot, P., Mele, F.,  
 811 Mocavero, S., Moulin, A., Müller, S., Nurser, G., Oddo, P., Paronuzzi, S., Paul, J., Peltier, M., Person, R., Rousset, C.,  
 812 Rynders, S., Samson, G., Schroeder, D., Storkey, D., Storto, A., Téchené, S., Vancoppenolle, M., and Wilson, C.: NEMO  
 813 Ocean Engine Reference Manual, <https://doi.org/10.5281/zenodo.14515373>, 2024.
- 814 Marin, M., Feng, M., Bindoff, N. L., and Phillips, H. E.: Local Drivers of Extreme Upper Ocean Marine Heatwaves  
 815 Assessed Using a Global Ocean Circulation Model, *Front. Clim.*, 4, <https://doi.org/10.3389/fclim.2022.788390>, 2022.
- 816 Martinez, E., Ganachaud, A., Lefevre, J., and Maamaatuaiahutapu, K.: Central South Pacific thermocline water circulation  
 817 from a high-resolution ocean model validated against satellite data: Seasonal variability and El Niño 1997–1998 influence, *J.*  
 818 *Geophys. Res. Oceans*, 114, <https://doi.org/10.1029/2008JC004824>, 2009.
- 819 Moisan, J. R. and Niiler, P. P.: The Seasonal Heat Budget of the North Pacific: Net Heat Flux and Heat Storage Rates (1950–  
 820 1990), *J. Phys. Oceanogr.*, 28, 401–421, [https://doi.org/10.1175/1520-0485\(1998\)028<0401:TSHBOT>2.0.CO;2](https://doi.org/10.1175/1520-0485(1998)028<0401:TSHBOT>2.0.CO;2), 1998.





- 821 Mumby, P., Chisholm, J., Edwards, A., Andrefouet, S., and Jaubert, J.: Cloudy weather may have saved Society Island reef  
 822 corals during the 1998 ENSO event, *Mar. Ecol. Prog. Ser.*, 222, 209–216, <https://doi.org/10.3354/meps222209>, 2001a.
- 823 Mumby, P., Chisholm, J., Edwards, A., Clark, C., Roark, E., Andrefouet, S., and Jaubert, J.: Unprecedented bleaching-  
 824 induced mortality in *Porites* spp. at Rangiroa Atoll, French Polynesia, *Mar. Biol.*, 139, 183–189,  
 825 <https://doi.org/10.1007/s002270100575>, 2001b.
- 826 Oliver, E. C. J., Donat, M. G., Burrows, M. T., Moore, P. J., Smale, D. A., Alexander, L. V., Benthuyssen, J. A., Feng, M.,  
 827 Sen Gupta, A., Hobday, A. J., Holbrook, N. J., Perkins-Kirkpatrick, S. E., Scannell, H. A., Straub, S. C., and Wernberg, T.:  
 828 Longer and more frequent marine heatwaves over the past century, *Nat. Commun.*, 9, 1324, [https://doi.org/10.1038/s41467-](https://doi.org/10.1038/s41467-018-03732-9)  
 829 018-03732-9, 2018.
- 830 Oliver, E. C. J., Benthuyssen, J. A., Darmaraki, S., Donat, M. G., Hobday, A. J., Holbrook, N. J., Schlegel, R. W., and Gupta,  
 831 A. S.: Marine Heatwaves, *Annu. Rev. Mar. Sci.*, 13, 313–342, <https://doi.org/10.1146/annurev-marine-032720-095144>,  
 832 2021.
- 833 Pagli, B., Izumo, T., Cravatte, S. E., Hopuare, M., Martinoni-Lapierre, S., Laurent, V., Menkes, C., Monselesan, D., and  
 834 Auffray, S.: The Diverse Impacts of El Niño and La Niña Events over the South Pacific and in French Polynesia, *J. Clim.*,  
 835 38, 2681–2701, <https://doi.org/10.1175/JCLI-D-24-0408.1>, 2025a.
- 836 Pagli, B., Izumo, T., Cravatte, S., Hopuare, M., Martinoni-Lapierre, S., Laurent, V., and Menkes, C.: Interannual Variations  
 837 in Tropical Cyclone Activity in the Central South Pacific: Is ENSO the Whole Story?, *J. Clim.*, 38, 4097–4116,  
 838 <https://doi.org/10.1175/JCLI-D-24-0582.1>, 2025b.
- 839 Paulson, C. A. and Simpson, J. J.: Irradiance Measurements in the Upper Ocean, *J. Phys. Oceanogr.*, 7, 952–956,  
 840 [https://doi.org/10.1175/1520-0485\(1977\)007<0952:IMITUO>2.0.CO;2](https://doi.org/10.1175/1520-0485(1977)007<0952:IMITUO>2.0.CO;2), 1977.
- 841 Schlegel, R. W., Oliver, E. C. J., and Chen, K.: Drivers of Marine Heatwaves in the Northwest Atlantic: The Role of Air–Sea  
 842 Interaction During Onset and Decline, *Front. Mar. Sci.*, 8, <https://doi.org/10.3389/fmars.2021.627970>, 2021.
- 843 Sen Gupta, A., Thomsen, M., Benthuyssen, J. A., Hobday, A. J., Oliver, E., Alexander, L. V., Burrows, M. T., Donat, M. G.,  
 844 Feng, M., Holbrook, N. J., Perkins-Kirkpatrick, S., Moore, P. J., Rodrigues, R. R., Scannell, H. A., Taschetto, A. S.,  
 845 Ummenhofer, C. C., Wernberg, T., and Smale, D. A.: Drivers and impacts of the most extreme marine heatwave events, *Sci.*  
 846 *Rep.*, 10, 19359, <https://doi.org/10.1038/s41598-020-75445-3>, 2020.
- 847 Skirving, W., Marsh, B., De La Cour, J., Liu, G., Harris, A., Maturi, E., Geiger, E., and Eakin, C. M.: CoralTemp and the  
 848 Coral Reef Watch Coral Bleaching Heat Stress Product Suite Version 3.1, *Remote Sens.*, 12, 3856,  
 849 <https://doi.org/10.3390/rs12233856>, 2020.
- 850 Stackhouse, P. W., Cox, S. J., Mikovitz, J. C., and Zhang, T.: GEWEX (Global Energy and Water Exchanges Project):  
 851 Surface Radiation Budget (SRB) Release 4 Integrated Product (IP4) - Algorithm Theoretical Basis Document and  
 852 Evaluation, 2021.
- 853 Van Wynsberge, S., Menkes, C., Le Gendre, R., Passfield, T., and Andréfouët, S.: Are Sea Surface Temperature satellite  
 854 measurements reliable proxies of lagoon temperature in the South Pacific?, *Estuar. Coast. Shelf Sci.*, 199, 117–124,  
 855 <https://doi.org/10.1016/j.ecss.2017.09.033>, 2017.
- 856 Van Wynsberge, S., Quéré, R., Andréfouët, S., Autret, E., and Le Gendre, R.: Spatial variability of temperature inside atoll  
 857 lagoons assessed with Landsat-8 satellite imagery, *Remote Sens. Appl. Soc. Environ.*, 36, 101340,  
 858 <https://doi.org/10.1016/j.rsase.2024.101340>, 2024.



- 859 Vincent, E. M., Lengaigne, M., Menkes, C. E., Jourdain, N. C., Marchesiello, P., and Madec, G.: Interannual variability of  
 860 the South Pacific Convergence Zone and implications for tropical cyclone genesis, *Clim. Dyn.*, 36, 1881–1896,  
 861 <https://doi.org/10.1007/s00382-009-0716-3>, 2011.
- 862 Vogt, L., Burger, F. A., Griffies, S. M., and Frölicher, T. L.: Local Drivers of Marine Heatwaves: A Global Analysis With an  
 863 Earth System Model, *Front. Clim.*, 4, <https://doi.org/10.3389/fclim.2022.847995>, 2022.
- 864 Watanabe, M., Kang, S. M., Collins, M., Hwang, Y.-T., McGregor, S., and Stuecker, M. F.: Possible shift in controls of the  
 865 tropical Pacific surface warming pattern, *Nature*, 630, 315–324, <https://doi.org/10.1038/s41586-024-07452-7>, 2024.
- 866 Whitaker, H. and DeCarlo, T.: Re(de)fining degree-heating week: coral bleaching variability necessitates regional and  
 867 temporal optimization of global forecast model stress metrics, *Coral Reefs*, 43, 969–984, [https://doi.org/10.1007/s00338-](https://doi.org/10.1007/s00338-024-02512-w)  
 868 [024-02512-w](https://doi.org/10.1007/s00338-024-02512-w), 2024.
- 869 Wyatt, A. S. J., Leichter, J. J., Washburn, L., Kui, L., Edmunds, P. J., and Burgess, S. C.: Hidden heatwaves and severe coral  
 870 bleaching linked to mesoscale eddies and thermocline dynamics, *Nat. Commun.*, 14, 25, [https://doi.org/10.1038/s41467-022-](https://doi.org/10.1038/s41467-022-35550-5)  
 871 [35550-5](https://doi.org/10.1038/s41467-022-35550-5), 2023.
- 872 Zaron, E. D.: Baroclinic Tidal Sea Level from Exact-Repeat Mission Altimetry, *J. Phys. Oceanogr.*, 49, 193–210,  
 873 <https://doi.org/10.1175/JPO-D-18-0127.1>, 2019.
- 874 Zhang, Y., Du, Y., Feng, M., and Hobday, A. J.: Vertical structures of marine heatwaves, *Nat. Commun.*, 14, 1–12,  
 875 <https://doi.org/10.1038/s41467-023-42219-0>, 2023.
- 876